

Whole-Brain Imaging with Single-Cell Resolution Using Chemical Cocktails and Computational Analysis

Etsuo A. Susaki,^{1,2,3,4,14} Kazuki Tainaka,^{1,3,4,14} Dimitri Perrin,^{2,14} Fumiaki Kishino,⁵ Takehiro Tawara,⁶ Tomonobu M. Watanabe,⁷ Chihiro Yokoyama,⁸ Hirotaka Onoe,⁸ Megumi Eguchi,⁹ Shun Yamaguchi,^{9,10} Takaya Abe,¹¹ Hiroshi Kiyonari,¹¹ Yoshihiro Shimizu,¹² Atsushi Miyawaki,¹³ Hideo Yokota,⁶ and Hiroki R. Ueda^{1,2,3,4,*}

¹Laboratory for Synthetic Biology, RIKEN Quantitative Biology Center

²Laboratory for Systems Biology, RIKEN Center for Developmental Biology
2-2-3 Minatojima-minamimachi, Chuo-ku, Kobe, Hyogo 650-0047, Japan

³Department of Systems Pharmacology, Graduate School of Medicine, The University of Tokyo, 7-3-1 Hongo, Bunkyo-ku, Tokyo 113-0033, Japan

⁴CREST, Japan Science and Technology Agency, 4-1-8 Honcho, Kawaguchi, Saitama, 332-0012, Japan

⁵Faculty of Medicine, The University of Tokyo, 7-3-1 Hongo, Bunkyo-ku, Tokyo 113-0033, Japan

⁶Image Processing Research Team, RIKEN Center for Advanced Photonics, 2-1 Hirosawa, Wako, Saitama, 351-0198, Japan

⁷Laboratory for Comprehensive Bioimaging, RIKEN Quantitative Biology Center, OLABB, Osaka University, 6-2-3, Furuedai, Suita, Osaka 565-0874, Japan

⁸Bio-Function Imaging Team, RIKEN Center for Life Science Technologies, 6-7-3 Minatojima-minamimachi, Chuo-ku, Kobe City, Hyogo 650-0047, Japan

⁹Division of Morphological Neuroscience, Gifu University Graduate School of Medicine, 1-1 Yanagido, Gifu City, Gifu 501-1194, Japan

¹⁰PRESTO, Japan Science and Technology Agency, 4-1-8 Honcho, Kawaguchi, Saitama, 332-0012, Japan

¹¹Laboratory for Animal Resources and Genetic Engineering, RIKEN Center for Developmental Biology, 2-2-3 Minatojima-minamimachi, Chuo-ku, Kobe, Hyogo 650-0047, Japan

¹²Laboratory for Cell-Free Protein Synthesis, RIKEN Quantitative Biology Center, 2-2-3 Minatojima-minamimachi, Chuo-ku, Kobe, Hyogo 650-0047, Japan

¹³Laboratory for Cell Function Dynamics, RIKEN Brain Science Institute, 2-1 Hirosawa, Wako, Saitama 351-0198, Japan

¹⁴Co-first author

*Correspondence: uedah-ky@umin.ac.jp

<http://dx.doi.org/10.1016/j.cell.2014.03.042>

SUMMARY

Systems-level identification and analysis of cellular circuits in the brain will require the development of whole-brain imaging with single-cell resolution. To this end, we performed comprehensive chemical screening to develop a whole-brain clearing and imaging method, termed CUBIC (clear, unobstructed brain imaging cocktails and computational analysis). CUBIC is a simple and efficient method involving the immersion of brain samples in chemical mixtures containing aminoalcohols, which enables rapid whole-brain imaging with single-photon excitation microscopy. CUBIC is applicable to multicolor imaging of fluorescent proteins or immunostained samples in adult brains and is scalable from a primate brain to subcellular structures. We also developed a whole-brain cell-nuclear counterstaining protocol and a computational image analysis pipeline that, together with CUBIC reagents, enable the visualization and quantification of neural activities induced by environmental stimulation. CUBIC enables time-course expression profiling of whole adult brains with single-cell resolution.

INTRODUCTION

Whole-brain imaging with single-cell resolution is one of the most important challenges in neuroscience, as it is required for system-level identification and analysis (Kitano, 2002) of cellular circuits in the brain. Various cross-sectional tomography methods have been developed to obtain high-resolution images throughout the brain (Gong et al., 2013; Li et al., 2010). Such section-based methods require expensive, specialized equipment, and the detailed structure between sections can be lost during sample processing. Alternatively, brain-transparentizing and -clearing techniques have been combined with rapid three-dimensional (3D) imaging using single-photon excitation microscopy, such as light-sheet fluorescence microscopy (LSFM) or specific plane illumination microscopy (SPIM). The 3D imaging can enable the study of systems from cells to organisms, such as cellular behavior in developing embryos and neural circuits in the adult brain (Dodt et al., 2007; Hägerling et al., 2013; Tomer et al., 2011). Such studies require a highly transparent sample for both illumination and detection.

Transparency is achieved by minimizing the light scattered by an object. Light is scattered at the boundary between materials with different refractive indices (RIs). Because lipids are a major source of light scattering in the fixed brain, the removal of lipids and/or adjustment of the RI difference between lipids and the surrounding areas are potential approaches for increasing brain

sample transparency. In an early trial of whole-brain imaging with macrozoom LSFM (Dodt et al., 2007), the brain tissue was cleared with BABB, a mixture of benzyl alcohol and benzyl benzoate. Because of BABB's hydrophobicity and because its high RI (1.56) (Becker et al., 2012) matched that of the fixed tissue, the sample was markedly cleared and suitable for observation with LSFM. Unfortunately, the clearing medium caused the rapid quenching of fluorescent signals. Although other organic chemical-based mixtures, such as tetrahydrofuran (THF) and dibenzyl ether (DBE) (Becker et al., 2012), performed somewhat better, some frequently used fluorescent proteins such as yellow fluorescent protein (YFP) were still quenched (Ertürk et al., 2012).

A hydrophilic chemical mixture called *Scale* was developed to clear brain samples (Hama et al., 2011). This urea-based reagent reduced quenching, and the resulting sample was suitable for both single-photon and multi-photon-based 3D tissue observation. Other issues, including relatively long sample treatment periods (weeks or months) and tissue swelling, were resolved by the development of another clearing reagent, SeeDB, which renders brain samples transparent within a few days by adjusting RI differences between the sample lipids and the surrounding tissue (Ke et al., 2013). SeeDB, a hydrophilic reagent lacking detergents or denaturation agents, preserves detailed structures as well as fluorescence signals. The remaining issue was that such simple hydrophilic reagents do not render whole-brain samples transparent enough for single-photon-based rapid whole-brain imaging. CLARITY, a recently reported technique for brain clearing (Chung et al., 2013), rendered brain samples transparent by aggressively removing lipids using electrophoresis. The resulting sample was highly transparent and suitable for LSFM imaging; however, use of a specialized electrophoresis device with a narrow range of optimal parameters makes parallelization and comparison among different samples difficult. Thus, although previous protocols have addressed some of the issues required for the efficient clearance of brain samples, an improved protocol was still required for whole-brain imaging with single-cell resolution.

The anatomical annotation of images is also critical. In conventional human brain imaging techniques such as computed tomography (CT) (Cormack, 1973), magnetic resonance imaging (MRI) (Lauterbur, 1973), and functional magnetic resonance imaging (fMRI) (Ogawa et al., 1990), anatomical annotation consists of two steps: (1) acquisition of whole-brain structural and specific signal (or functional) images and (2) computational analysis of these images. For example, fMRI, which visualizes neural activity, is almost always accompanied by MRI, which acquires a structural image of the whole brain. This image is then used for image registration and alignment to a standard whole-brain image ("reference brain") so that signal images can be compared across individuals. Because computational image analysis is so essential, informatics tools have been developed and implemented to facilitate this process in conventional human brain imaging (Avants et al., 2011). However, this kind of computational image analysis is rare for fluorescence imaging of whole mammalian brains due to the lack of whole-tissue histological counterstaining of cell nuclei,

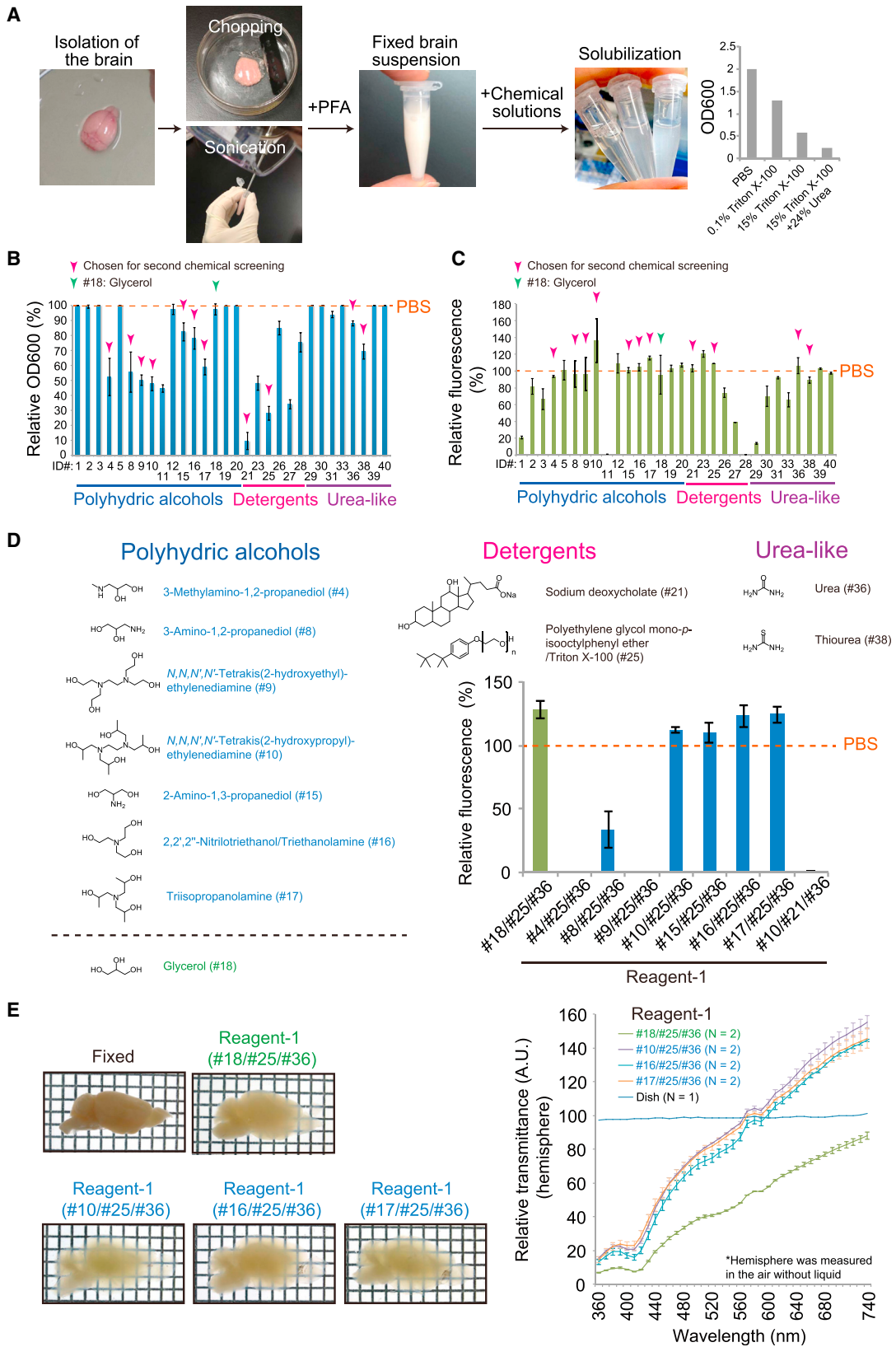
which can be used for anatomical orientation. 3D images acquired with sectional tomography or tissue-clearing protocols provide information on fluorescently labeled cells, but not on the overall shape and characteristic anatomical structures that are required for the registration and alignment steps. Even in a trial in which the image registration step was successful, manual determination of landmark structures was necessary (Gong et al., 2013). The larger number of images generated in time-course experiments makes the need for automated processing even more acute. Thus, efficient anatomical annotation will be required for whole-brain imaging with single-cell resolution.

We have developed a simple, efficient, and scalable brain-clearing method and computational analysis pipeline, CUBIC (clear, unobstructed brain imaging cocktails and computational analysis), that enables rapid whole-brain imaging with single-photon excitation microscopy. CUBIC can be applied to whole-brain imaging of various fluorescent proteins and 3D imaging of immunostained adult brain samples. CUBIC is scalable from primate brain imaging to subcellular structures such as axons and dendritic spines. In order to facilitate interindividual comparisons, we have also developed an anatomical annotation method using a whole-brain cell-nuclear counterstaining protocol and a computational image analysis pipeline. CUBIC enables the time-course expression profiling of adult whole brains with single-cell resolution.

RESULTS

Development of CUBIC Reagents by Comprehensive Chemical Screening

To develop a simple, efficient, and scalable tissue-clearing protocol for whole-brain imaging, we started by rescreening the chemical components of the hydrophilic brain-clearing solution *ScaleA2* (Hama et al., 2011). We started with this protocol because of its ease and its ability to preserve fluorescent signals. We considered 40 chemicals, including polyhydric alcohols, detergents, and hydrophilic small molecules (Table S1 available online), corresponding to the components of the *ScaleA2* solution: glycerol, Triton X-100, and urea. To evaluate the clearing efficiency of these chemicals, we first sought to improve the experimental throughput of clearing measurements. In a typical evaluation procedure, we first fix, isolate, and immerse a whole mouse brain in one chemical mixture and then evaluate the clearing efficiency of the chemical by measuring the transmittance of the fixed, cleared whole brain. For a more efficient evaluation protocol, we exchanged the order of the fixation and isolation steps and introduced a homogenization step so that many chemicals can be tested using only one mouse brain (Figure 1A and Extended Experimental Procedures). This "solubilization" assay using a homogenized suspension instead of a whole brain enabled the reproducible, quantitative, and comprehensive evaluation of chemicals for their ability to dissolve brain tissue (Figure 1B). We also evaluated the quenching effect of each chemical on EGFP fluorescence in this first chemical screening (Figure 1C). We noted that a series of aminoalcohols (#4, #8, #9, #10, #15, #16, #17) showed considerable brain tissue solubilizing activity,



(legend on next page)

whereas polyhydric alcohols without amino groups (#1, #2, #3, #5, #12, #18, #19, #20) exhibited much less activity (Figure 1B and Table S1). This may indicate that the cationic amino group contributes to solvating anionic phospholipids, the most abundant lipids in the brain. In addition, basic aminoalcohols preserved and even enhanced EGFP fluorescent signals, whereas some weakly acidic amine-free alcohols (#1, #2, #3, #11) quenched the fluorescence (Figure 1C and Table S1). Many fluorescent proteins, such as EGFP, EYFP, and mCherry, contain a phenolate chromophore, which is highly pH sensitive, resulting in increased fluorescence intensity with increasing pH (until the protein denatures) (Kneen et al., 1998). In a highly concentrated aqueous medium without buffers, basic aminoalcohols were therefore more suitable clearing agents than other weakly acidic or neutral alcohols. After a second chemical screening (Figures 1D and 1E), our cocktail finally included *N,N,N',N'*-tetrakis(2-hydroxypropyl)ethylenediamine (#10), Triton X-100 (#25), and urea (#36) (Figure S1B). We refer to this first CUBIC reagent as ScaleCUBIC-1 (hereafter denoted as reagent 1). We used the words “Scale” and “CUBIC” because this reagent is based on urea (Scale) and aminoalcohols (CUBIC), respectively.

Reagent 1 treatment of the whole adult mouse brain resulted in a highly transparent brain (Figures 2A and 2B). The lipid-rich white matter was not completely cleared, possibly due to incomplete lipid removal and unmatched RIs between the tissue and solution. ScaleCUBIC-2 (hereafter denoted as reagent 2) was developed by modifying the reagent 1 recipe in a third chemical screening (Figure S1A). Addition of a high concentration of sucrose instead of glycerol increased the reagent RI (from 1.45–1.46 for glycerol-based reagent 2 to 1.48–1.49 for sucrose-based reagent 2, which is similar to the RI of SeeDB [RI = 1.49] [Ke et al., 2013]) so that it matched the tissue RI and increased the transmittance (Figure S1A). Replacing chemical #10 with 2,2',2''-nitrioltriethanol (#16) also reproducibly increased the transmittance (Figure S1A), motivating its inclusion in the final version of reagent 2 (Figures 2A and S1B). As expected, reagent 2 enhanced the optical clearance of lipid-rich regions deeper in the brain (Figure 2A).

CUBIC Is a Simple and Efficient Procedure

As summarized in Figure 2A, the CUBIC protocol involves a series of immersion steps followed by a washing step. The CUBIC brain samples were sufficiently transparent for adult whole-brain imaging. The sample was slightly swollen by reagent 1 treatment but returned to its original size following reagent 2 treatment. In addition, CUBIC-based clearing can be used to clear an acrylamide gel-embedded sample prepared according to the CLARITY protocol (Chung et al., 2013), addressing concerns about destruction of detailed anatomical structures and protein loss (Figure S1C).

Sample clearing with CUBIC reagents required 2 weeks for completion, comparable to CLARITY (~10 days) (Chung et al., 2013) and faster than ScaleA2 (weeks) and ScaleU2 (months) (Hama et al., 2011). Although clearing with 3DISCO can be completed in 5 days, fluorescence signals are quenched within a few days of preparation (Ertürk et al., 2012). To evaluate the quenching effect of CUBIC, we next incubated various recombinant fluorescent proteins with reagent 1, reagent 2, or PBS for 24 hr or 7 days (Figure 2C). The fluorescence of all of the tested proteins, even EYFP, the most sensitive, remained high after the 7-day incubation. The CUBIC protocol achieved comparable transparency to other recently developed methods in a reasonable time, with minimal quenching of fluorescence signals. Notably, the red fluorescent proteins mCherry and mKate2 also showed minimal quenching. Given that red light transmits through tissues more efficiently than shorter wavelength light (Figure 2B), these proteins are very suitable as labeling tools for use with the CUBIC protocol.

To confirm that CUBIC samples can be used for deep brain imaging, we performed two-photon imaging of a Thy1-YFP-H Transgenic (Tg) mouse brain (Feng et al., 2000) with an objective lens optimized for use with SCALEVIEW-A2 (working distance 8 mm, optimized for RI = 1.38) (Figure 2D). We treated a hemisphere with reagent 1 for 3 days and acquired a Z stack image. Treatment with reagent 1 alone was sufficient for deep brain imaging (up to ~4 mm) with two-photon excitation microscopy (Figure 2D). The accelerated clearing obtained with reagent 1 enabled substantially deep brain imaging up to ~4 mm, whereas

Figure 1. Development of CUBIC Reagents by Comprehensive Chemical Screening

(A) Method for screening chemicals for brain-solubilizing activity using a fixed brain suspension. Turbidity of the suspension was quantitatively determined with an absorptiometer and was expressed as an OD600 value. See also [Extended Experimental Procedures](#) and [Table S1](#).

(B) Solubilization assay. The fixed brain suspension was mixed and incubated with 10 wt% aqueous solutions of candidate chemicals. After 24 hr, the mixtures were subjected to OD600 measurement.

(C) EGFP quenching assay. Recombinant EGFP was incubated in 10 wt% aqueous solutions of candidate chemicals for 12 hr, after which the fluorescence signals were measured.

In (B) and (C), the data represent the average (\pm SD) of two independent measurements. Chemicals without ID number were rejected before the step due to their low solubility (<10 wt%) or unavailability (see [Table S1](#)). Chemicals chosen for the second chemical screening in (D) and glycerol (#18) are indicated with magenta arrowheads and a green arrowhead, respectively.

(D) Second chemical screening of candidate chemicals for reagent 1. The EGFP quenching assay was performed with the final recipe of reagent 1 (Figure S1B). Fluorescent signal intensities were measured as in (C), and the average relative fluorescence \pm SD of two independent measurements is shown in the graph. #38 was rejected due to its relatively low solubility (<15 wt% in water).

(E) Effect of using aminoalcohols instead of glycerol in reagent 1. From the results in (D), we chose aminoalcohols (#10, #16, #17), Triton X-100 (#25), and urea (#36) for further evaluation. Glycerol (#18) was also tested as a Scale-based mixture, as in (D). #15 was rejected due to its cost and safety concerns (see [Table S1](#)). Fixed mouse hemispheres were subjected to clearing with the indicated solutions for 3 days followed by measurement of transmittance (360–740 nm). The transmittance data are shown as relative transmittance, normalized to the blank, defined as 100. The values in the graph represent the average \pm SEM from two independent samples. Note that some of the values exceeded 100, possibly due to the difference in the RI of the sample and the surrounding air (see [Extended Experimental Procedures](#)).

See also [Figure S1](#).

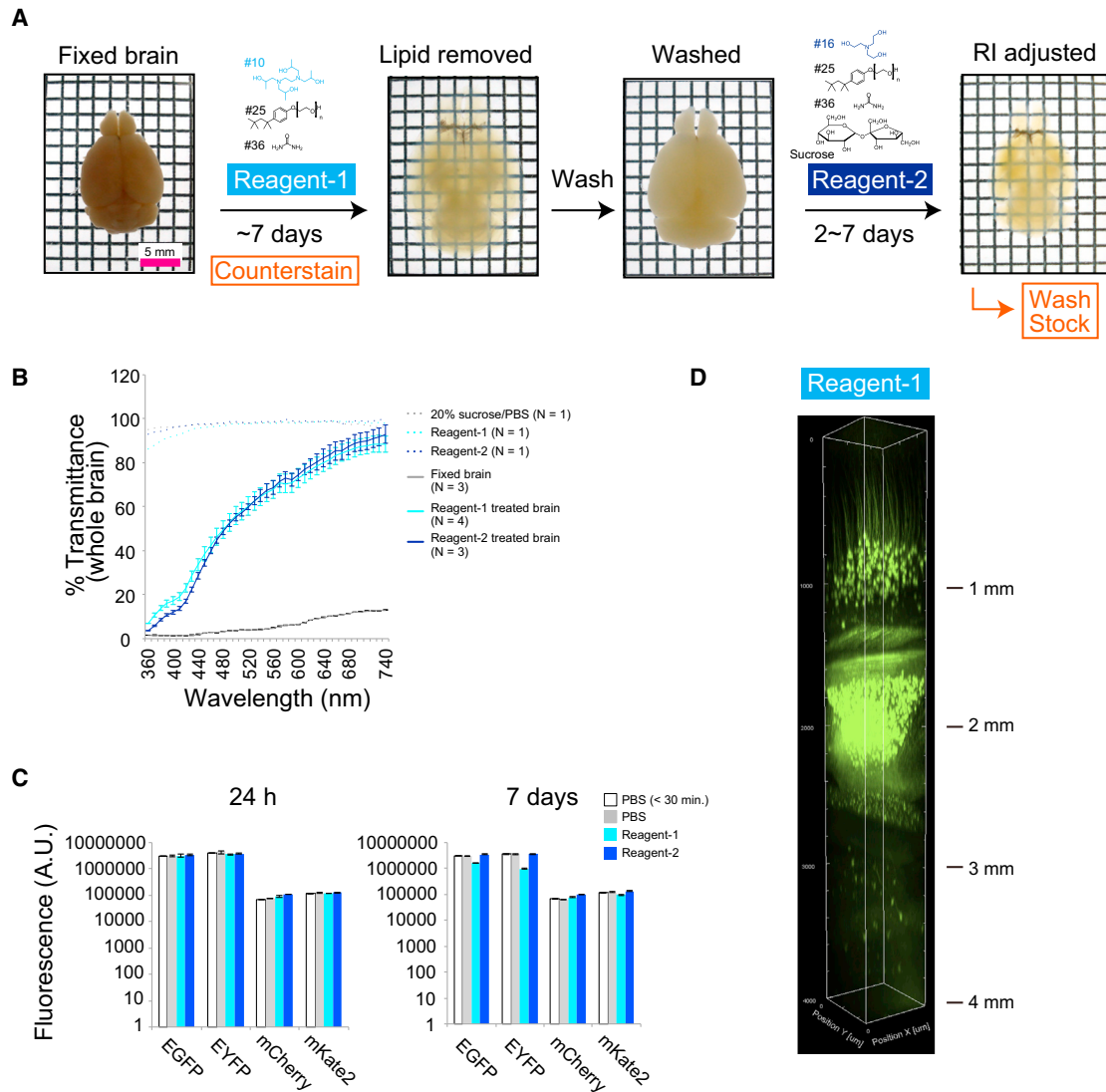


Figure 2. CUBIC, A Simple and Efficient Whole-Brain Clearing Protocol

(A) CUBIC protocol. A fixed whole brain (from a 6-month-old mouse) was treated with reagent 1 to remove lipid components for up to 7 days, followed by washing with PBS. The sample was then treated with reagent 2 for 2–7 days to adjust the refractive indices of the tissue and reagent. Optional procedures are indicated in orange boxes: nuclear counterstaining during reagent 1 treatment, and sample storage at 4°C or –80°C after completion.

(B) Transmission curves. Light transmittance (360–740 nm) of fixed whole brain (n = 3), reagent-1-treated whole brain (day 7, n = 4), reagent-2-treated whole brain (day 3, n = 3), and the corresponding reagents (n = 1, for each reagent) were measured and normalized to the blank. Data shown represent the average \pm SEM.

(C) Quenching test of fluorescent proteins by CUBIC reagents. The indicated recombinant fluorescent proteins were incubated in each reagent or PBS for 24 hr or 7 days, followed by measurement of the fluorescent signal intensity. Data shown represent the average \pm SD of three independent measurements.

(D) Two-photon deep brain imaging of a reagent-1-treated Thy1-YFP-H Tg hemisphere. A single hemisphere was treated with the reagent 1 for 3 days at 37°C. The resulting sample was observed using two-photon microscopy.

See also Figure S2.

SCALEVIEW-A2-treated samples became transparent more slowly (Figure S2).

CUBIC Enables Rapid, High-Performance, Whole-Brain Imaging with LSFM

The high transparency of CUBIC samples and the two-photon imaging results prompted us to perform whole-brain imaging

with single-photon excitation microscopy techniques such as LSFM. Previous reports have used confocal- or multi-photon-based imaging methods (Chung et al., 2013; Ke et al., 2013), in which image tiling and data acquisition time (days for a single brain) were significant challenges. LSFM, which enables rapid whole-brain imaging, was used in a previous study using BABB (Dodt et al., 2007), though fluorescence signal loss

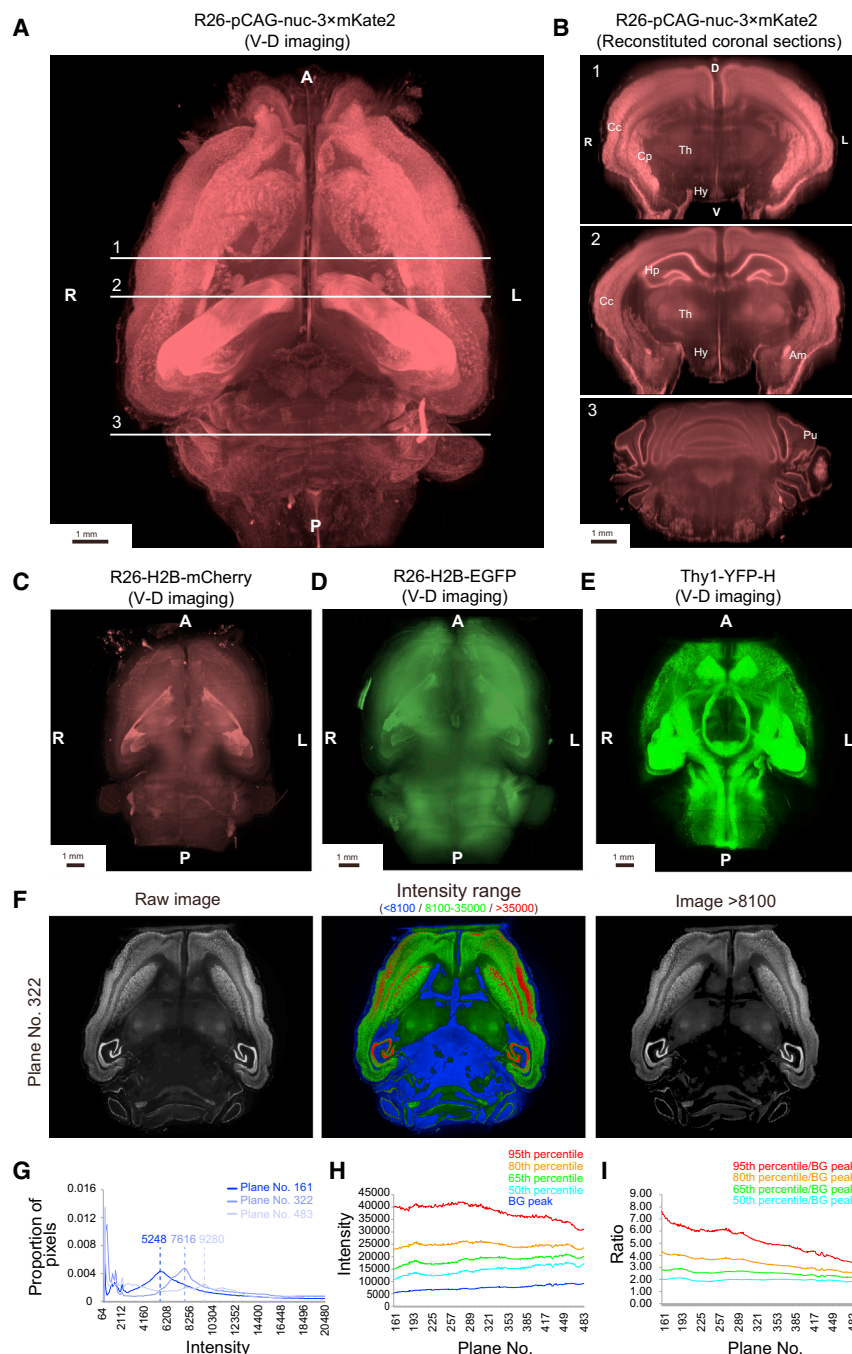


Figure 3. CUBIC Can Be Used for Rapid and High-Performance Whole-Brain Imaging of Various Fluorescent Proteins

3D-reconstituted images of mouse brains expressing various fluorescent proteins were acquired with LSFM. A, anterior; P, posterior; R, right; L, left; D, dorsal; V, ventral. Ventral view is shown.

(A) R26-pCAG-nuc-3 × mKate2 mouse brain (5-week-old mouse). Images were acquired from the ventral-to-dorsal (V-D) direction. Z stack: 10 μm step × 646 planes, with 0.28 s × two illuminations. (B) Reconstituted coronal sections at the indicated positions (1–3) shown in (A). Cc, cerebral cortex; Cp, caudoputamen; Th, thalamus; Hy, hypothalamus; Hp, hippocampus; Am, amygdala; Pu, Purkinje cell layer. (C) V-D image of a R26-H2B-mCherry mouse brain (6-month-old mouse). Z stack: 10 μm step × 709 planes, with 4 s × two illuminations.

(D) V-D image of a R26-H2B-EGFP mouse brain (6-month-old mouse). Z stack: 10 μm step × 665 planes, with 4 s × two illuminations. (E) V-D image of a Thy1-YFP-H Tg mouse brain (2-month-old mouse). Z stack: 10 μm step × 696 planes, with 0.3 s × two illuminations. See also Figure S3 and Movie S1.

(F) (Left) Raw TIFF image from plane 322 of the R26-pCAG-nuc-3 × mKate2 mouse brain. (Center) False-color image highlighting regions with intensity <8,100 (blue), between 8,100 and 35,000 (green), and >35,000 (red). In each channel, brighter colors mean higher intensity within the range in the raw image. (Right) Processed image for plane 322, where all pixels whose intensity is below 8,100 are set to black.

(G) Low-intensity peaks (corresponding to background peaks) in the TIFF image histogram, shown for planes 161, 322, and 483. (H) Background peaks (BG peak) and percentiles for the intensity distribution of pixels whose intensity is at least 5% higher than BG peak. (I) Ratios between the percentiles and the background peaks shown in (H).

(G) Low-intensity peaks (corresponding to background peaks) in the TIFF image histogram, shown for planes 161, 322, and 483.

(H) Background peaks (BG peak) and percentiles for the intensity distribution of pixels whose intensity is at least 5% higher than BG peak.

(I) Ratios between the percentiles and the background peaks shown in (H).

photostability, and rapid protein maturation (Chudakov et al., 2010), as well as its resistance to fluorescence quenching by CUBIC reagents (Figure 2C).

We then collected Z stack images of the horizontal section (Movie S1) of a CUBIC whole brain from two directions (dorsal to ventral, D-V, and ventral to dorsal, V-D).

With our current microscope setup, imaging took 30 min to 1 hr per brain/color/direction. The reconstituted 3D whole-brain image of the mKate2 knockin mouse (Figures 3A and S3B) and its virtual coronal sections (Figure 3B) enabled the 3D visualization of spatial gene expression patterns and the examination of detailed internal structures. Furthermore, we confirmed that background fluorescence in CUBIC samples is low enough not to impair visualization of the fluorescent signal from mKate2 in the overall brain image data (Figures 3F–3I and Extended Experimental Procedures).

over time was a problem. We first set up an optimized macro-zoom microscope combined with a light-sheet illuminator (LaVision Ultramicroscope) (Figure S3A) so that an entire horizontal section of a mouse brain can be acquired in a single plane with subcellular resolution (theoretical X-Y resolution in the acquired image is 4.7 μm). For rapid whole-brain imaging, we generated a knockin mouse strain expressing three tandem repeats of *mKate2* with a nuclear localization signal, under control of the CAG promoter (Niwa et al., 1991) from the ROSA26 locus. We used mKate2 because of its signal intensity,

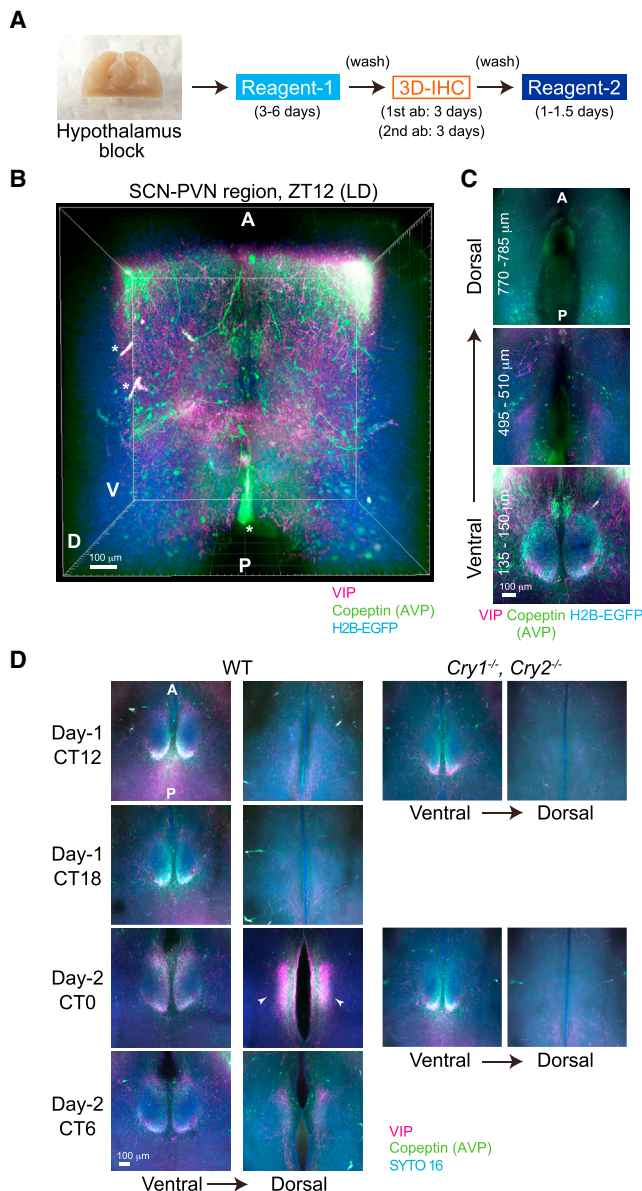


Figure 4. CUBIC Can Be Used for Imaging of 3D Immunostained Adult Brain Samples

(A) CUBIC treatment procedure and 3D immunohistochemistry (3D-IHC) of a hypothalamus block with anti-VIP and -Copeptin antibodies (1st ab) and Alexa-conjugated second antibodies (2nd ab).

(B) 3D view of the SCN region of R26-H2B-EGFP mouse. Sampling was performed at zeitgeber time 12 (ZT12) under 12 hr:12 hr light-dark conditions. Horizontal images were acquired from the ventral side with an inverted confocal microscope (Z stack: 4.99 μm step \times 173 planes). A, anterior side; P, posterior side; D, dorsal side; V, ventral side. Asterisks indicate nonspecific signals in the third ventricle and the vessels.

(C) Selected horizontal images (Z projection with maximum intensity, 4.99 μm step \times 3 planes) from (B). Approximate depth from the first image of the Z stack data are indicated.

(D) 3D-IHC results of the WT and *Cry1*^{-/-}, *Cry2*^{-/-} SCN, collected at different time points under constant dark conditions. Nuclear counterstaining with SYTO 16 was performed during reagent 1 treatment. Depth of the horizontal images was \sim 140 μm on the ventral side and 290 μm on the dorsal side

CUBIC Is Applicable to the Whole-Brain Imaging of Various Fluorescent Proteins

Our successful imaging using mKate2 led us to test other fluorescent proteins, including mCherry, EGFP, and YFP. We performed similar whole-brain imaging with CUBIC adult whole brains from three mouse strains: an mCherry-fused histone-2B-expressing strain (R26-H2B-mCherry [CDB0239K]; Figures 3C and S3C; Abe et al., 2011), an EGFP-fused histone-2B-expressing strain (R26-H2B-EGFP [CDB0238K]; Figures 3D and S3D; Abe et al., 2011), and a Thy1-YFP-H transgenic strain (Figures 3E and S3E). By comparing the reconstituted sections of these samples, spatial gene expression patterns and their differences across samples could be easily traced. For example, we compared two knockin strains in which the gene was inserted into the same ROSA26 locus but regulated by different promoters; the gene for mKate2 was regulated by the CAG promoter and, for mCherry, by the endogenous ROSA26 promoter. The whole-brain image showed expression differences in regions such as the thalamus, hypothalamus, midbrain, granular layer of the cerebellum, and ventricular choroid plexus (Figures S3F and S3G). These results show that various fluorescent proteins can be used for rapid and high-performance whole-brain imaging with the CUBIC protocol.

CUBIC Is Applicable to Adult Brain Imaging of 3D-Immunostained Samples

Given that CUBIC samples were highly permeabilized by lipid removal, we predicted that the CUBIC protocol would be useful for the immunostaining of large blocks of brain tissue, a potential improvement over sectional staining. We performed 3D immunohistochemistry (3D-IHC) using a brain block containing the hypothalamus region (Figure 4A). The block was subjected to reagent 1 treatment, followed by 3D-IHC with antibodies to neuropeptides expressed in the suprachiasmatic nucleus (SCN), the central clock of the mammalian circadian system. We used antibodies for Copeptin (a peptide cleaved from the common precursor of arginine vasopressin [AVP]; Land et al., 1982) and for vasoactive intestinal peptide (VIP) to label the AVP and VIP neurons in the nucleus. After immunostaining, the block was treated with reagent 2 for further clearing, and the resulting sample was observed with an inverted single-photon confocal microscope. We imaged a horizontal plane of the SCN and paraventricular nucleus (PVN) regions of the hypothalamus from the bottom of the brain. The immunostained signals were detected at a depth of $>750 \mu\text{m}$ (from the bottom of the brain to the dorsal area of the PVN in the hypothalamus) and were visualized as a 3D reconstituted image (Figure 4B and Movie S2). In the acquired horizontal images, the cell bodies and fibers of the two types of neurons were clearly visible (Figure 4C). High-resolution images were also included (Figure S4C). Abrahamson and Moore have

(Z projection with maximum intensity, 1.98 μm step \times 3 planes) from the most ventral plane of the SCN region. Strong signals for the neuropeptides were detected on the dorsal side of the WT SCN at CT0 of day 2 (arrowheads), which were barely detected in the *Cry1*^{-/-}, *Cry2*^{-/-} SCN. Images were acquired and processed in a similar but optimized condition for each sample so that most of the stained signals were obtained in the unsaturated range of intensity.

See also Figure S4 and Movies S2–S4.

demonstrated that a large number of VIP-positive soma were densely packed in the ventral area of the SCN and that AVP-positive soma were localized in the dorsomedial and ventrolateral area of the SCN and dorsally distributed even around the paraventricular nucleus (Abrahamson and Moore, 2001). The ventral image at a depth of ~ 45 μm (including the most ventral area of the SCN) displayed extensive VIP-positive soma signals in the left panel of Figure S4C. The middle image at a depth of ~ 65 μm (including the more dorsal area of the SCN) exhibited AVP-positive soma and VIP-positive fibers in the middle panel of Figure S4C. The dorsal image at a depth of ~ 780 μm (including the paraventricular nucleus) included sparse AVP-positive soma in the right panel of Figure S4C. Therefore, previously reported spatial distributions of AVP- and VIP-positive soma and fibers were clearly recapitulated by CUBIC-based 3D IHC.

We further applied 3D-IHC analysis to the SCN of both wild-type (WT) and a *Cry1^{-/-}, Cry2^{-/-}* clock gene double-knockout strain (van der Horst et al., 1999), sacrificed at different circadian times (CT). For these samples, nuclear counterstaining with SYTO 16, a cell-permeable green fluorescent nucleic acid stain, was performed during the reagent 1 treatment. Plane images at different depths (Figures 4D and S4A) and reconstituted 3D images (Movies S3 and S4) showed CT-dependent differences in the staining patterns of these two neuropeptides. The most striking difference was that the fibers in the dorsal region of the SCN were more strongly stained at CT0 than at other circadian times. This tendency was reproduced in an independent set of experiments (Figure S4A) as well as in animals housed under light-dark conditions (Figure S4B). These differences were not observed in images of the *Cry1^{-/-}, Cry2^{-/-}* strain captured at CT0 and CT12 (Figures 4D and S4A), suggesting that the observed immunostaining differences in the AVP and VIP neurons were dependent on the circadian clock. The CUBIC protocol is highly applicable to the 3D imaging of immunostained adult-brain blocks.

CUBIC Is Scalable from Subcellular Structures to a Primate Brain

In addition to the efficiency of the CUBIC protocol, its scalability is also important for a wide range of applications. One potential application of a brain-clearing protocol is to trace neural connections at the axon or synapse level. We therefore tested whether detailed cell structures such as axons and spines were preserved in CUBIC samples. We used Thy1-YFP-H transgenic mice in which neuronal subcellular structures, including somata, axons, and dendritic spines, can be labeled and visualized by YFP fluorescence (Feng et al., 2000). A magnified view of a CUBIC brain sample from the Thy1-YFP-H transgenic mouse revealed that the axons and somata of neurons were well preserved (the pontine-medullary region in the LSFM image is shown in Figure S5A). A single axon was labeled and visualized without any breaks, making its trajectory easily traceable. In addition, the dendritic spines in the cerebral cortex of the same strain were clearly observed by two-photon microscopy (Figure S5B). Furthermore, proteins in the spine were also preserved in the CUBIC sample by immunostaining with an antibody against synapsin I, a phosphoprotein associated

with synaptic vesicles in neural synapses (Navone et al., 1984) (Figure S5C). Synaptic proteins were preserved in the CUBIC samples, suggesting that CUBIC is scalable to subcellular structure imaging.

Another potential application for a brain-clearing protocol is in primate whole-brain imaging. The marmoset is becoming an increasingly popular primate model organism in neuroscience because of its potential for genetic engineering (Sasaki et al., 2009). We tested whether the CUBIC protocol is applicable to marmoset whole-brain fluorescence imaging with nuclear counterstaining. A postnatal-day-3 marmoset brain has ~ 10 times the volume of an adult mouse brain (Figure 5A). CUBIC treatment with SYTO 16 staining of the hemisphere from a 3-day-old marmoset resulted in clearing comparable to that achieved with the mouse brain (a hemisphere was used instead of a whole marmoset brain due to the size limitation of the microscope stage used in this study; Figure 5B). The acquired raw images were subjected to 3D image reconstitution to generate a volume-rendering image (Figures 5C and 5D) and reconstituted sections (Figure 5E). The reconstituted image clearly depicts general and detailed structures of the marmoset brain, such as vessels and layers of the cerebral cortex (Figures 5C–5E and Movie S5). These results suggest that the CUBIC protocol is scalable to larger tissues, indicating its potential application to various animals, including primates. Together, the CUBIC protocol is scalable from subcellular structures to a primate brain, a feature that will support wide-ranging applications in neuroscience.

Whole-Brain Nuclear Counterstaining and Computational Image Analysis in CUBIC Enable the Visualization of Neural Activities Induced by Environmental Stimulation with Single-Cell Resolution

Another challenge for establishing whole-brain imaging with single-cell resolution is the development of anatomical annotation. For this purpose, we used Arc-dVenus transgenic mice, in which an unstable Venus protein is expressed under the control of a neural activation marker gene, *Arc* (Eguchi and Yamaguchi, 2009). Arc-dVenus transgenic mice were housed under constant dark conditions for about 2.5 days and were then exposed to constant light at CT2.5, followed by fixation and collection of their brains (Figure 6A). As previously reported, light-dependent neural activation was observed with fluorescent stereomicroscopy, showing increased Venus signals in the visual area of the cortex in a light-exposed brain (Figure S6A, Light+ (1)), compared with a control brain (Figure S6A, Light–).

Because anatomical annotation requires the acquisition of whole-brain structural images, we performed nuclear counterstaining with propidium iodide (PI) to acquire whole-brain structural images in the red channel. The brain samples were subjected to CUBIC treatment with PI counterstaining, and the resulting samples were analyzed by whole-brain imaging with LSFM. The reconstituted 3D images clearly revealed light-responsive neurons, such as those in the visual area (Vi) (Figures 6B and 6C and Movies S6 and S7). Individual neurons were clearly visible, suggesting that the whole-brain image achieved single-cell resolution. Several additional brain regions, including the orbital area (Or), the motor area (Mo), the anterior cingulate area (Ac), the

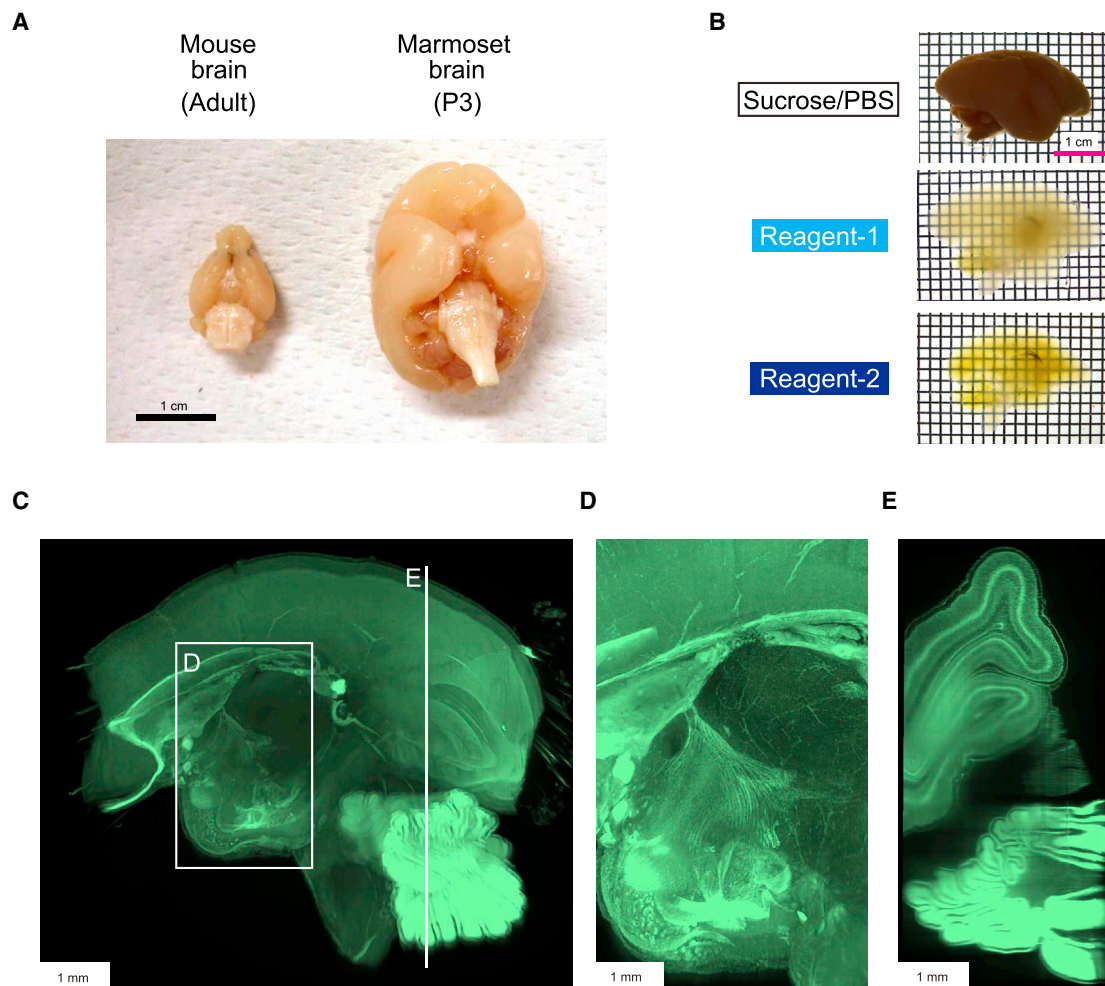


Figure 5. CUBIC Is Scalable to a Primate Brain

(A) Comparison of the size of an adult mouse brain and a postnatal day 3 (P3) marmoset brain.

(B) CUBIC treatment and SYTO 16 nuclear staining of the marmoset hemisphere. The images of the same marmoset hemisphere after reagent 1 and reagent 2 treatments are shown.

(C–E) A 3D-reconstituted fluorescent image of the nuclear-stained marmoset hemisphere (Z stack: 10 μm step \times 900 planes, with 0.25 s \times two illuminations) acquired with LSM. Magnified view of the boxed region in (C) is shown in (D). A reconstituted coronal section at the indicated position in (C) is shown in (E). Anatomical structures such as vessels and layers of the cerebral cortex can be observed in the reconstituted images.

See also [Figure S5](#) and [Movie S5](#).

orbital area, and subcortical areas in the forebrain (such as the claustrum and endopiriform nucleus [Cl/Ep]), also exhibited increased Venus signals in the light-exposed brain ([Figure 6B](#)), compared to the control brain ([Figure 6C](#)). These areas are known to be connected to each other and to respond to several sensory stimuli ([Miller and Vogt, 1984](#); [Reep et al., 1996](#); [Sloniewski et al., 1986](#)). This result was reproduced in another light-exposed brain (Light+ (2) in [Figures S6A](#) and [S6B](#)).

We next focused on the development of a computational image analysis pipeline (“CUBIC informatics,” [Figure 7A](#)). We first combined whole-brain images of the same brain that had been captured from two opposite directions (dorsal-to-ventral [D-V] and ventral-to-dorsal [V-D]) ([Figures S7A](#) and [S7B](#)). This was necessary because whole-brain images

captured from the dorsal-to-ventral direction (D-V images) were clear on the dorsal side but blurred on the ventral side and vice versa ([Figures S7C](#) and [S7E](#), V-D image and D-V image). To combine the two images, we first aligned them ([Figure S7A](#)) and then generated a single whole-brain image by considering the sharpness of each horizontal plane ([Figure S7D](#)). The blurred areas were compensated for in the combined image ([Figure S7E](#), combined image), which was used for subsequent computational analysis.

Applying this pipeline to Arc-dVenus transgenic mouse brains, we aligned the combined PI image of an internal reference brain (Light–) to a reference brain ([Figure 7B](#)), aligned the PI images captured from the Light+ and Light– brains ([Figure 7C](#)), and directly compared the dVenus fluorescence signals of these

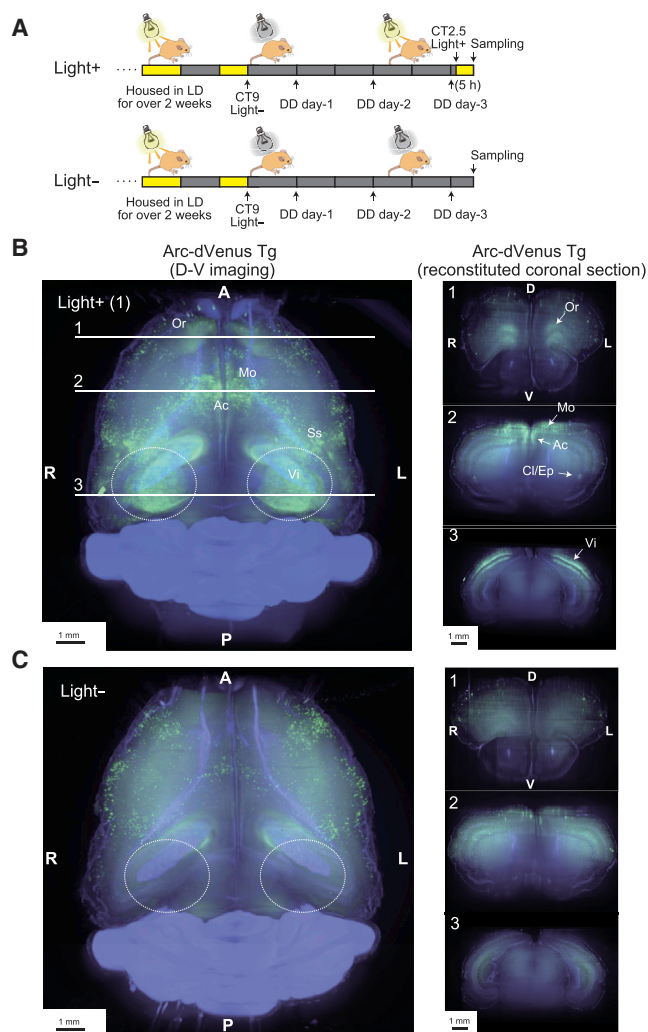


Figure 6. Whole-Brain Nuclear Counterstaining in CUBIC Enables the Visualization of Neural Activities Induced by Environmental Stimulation

(A) Experimental scheme. Arc-dVenus Tg mice (11 weeks old) housed under constant dark (DD) conditions for about 2.5 days were then stimulated by light (Light+) or maintained in the dark (Light-) and were sacrificed 5 hr after stimulation.

(B and C) Whole-brain images and reconstituted coronal sections (indicated positions in the whole brain image in (B)) of CUBIC brains from Light+ (1) and Light- mice, corresponding to Figure S6A. The brains were stained with PI (light purple), and two-color D-V images were acquired with LSFM (Z stack: 10 μ m step \times 625 planes for B and 10 μ m step \times 648 planes for C, with 3 s \times two illuminations for Venus and with 0.3 s \times two illuminations for PI, respectively). A region including the visual area is indicated by the dotted ellipse. Areas where Venus signals were increased in the Light+ brain are indicated in the whole-brain image and reconstituted coronal sections in (B). Or, orbital area; Mo, motor area; Ac, anterior cingulate area; Ep, endopiriform nucleus; Cl, claustrum; Vi, visual area; Ss, somatosensory area. See also Figure S6 and Movies S6 and S7.

brains by overlaying their aligned images (Figure 7D). Subtraction of the signal intensities clearly showed the brain regions stimulated by light (Figure 7E). These regions included areas

identified in Figures 6B and S6B but with improved clarity due to the sharper combined image. The CUBIC protocol combined with CUBIC informatics enables gene expression profiling of adult whole brains.

DISCUSSION

CUBIC Is a Simple, Efficient, and Scalable Protocol of Wide Applicability

The CUBIC protocol appears to have reconciled some of the seemingly incompatible demands of previous methods. First, it is simple in that it requires only the immersion of tissue in two reagents for relatively short periods (Figure 2). Simplicity is advantageous for multi-sample imaging. The water-based Scale and SeeDB methods also have simple protocols, though the resulting sample transparency is insufficient for rapid whole-brain imaging of the adult brain. 3DISCO and CLARITY produce highly transparent brain samples but require careful handling of reagents or specialized devices. CLARITY also requires expensive clearing reagents such as *FocusClear* for final clearing before imaging. In contrast, CUBIC produced a highly transparent brain specimen at lower cost (Table S1) and using nontoxic water-soluble chemicals. Second, the CUBIC protocol can be used with many different types of fluorescent proteins (Figures 3 and 6) and to compare multiple samples by 3D-IHC (Figure 4). This efficient and highly reproducible method also enabled time-course expression profiling with single-cell resolution. Third, the CUBIC protocol is scalable, as it achieved transparentization of a larger primate brain (Figure 5) while preserving detailed subcellular structures such as the axons and spines of neurons (Figure S5). CUBIC reagents can also be used to clear acrylamide-gel-embedded samples prepared according to the CLARITY protocol (Chung et al., 2013), if necessary (Figure S1C). The CUBIC protocol and reagents have the potential to be modified or optimized based on specific sample or experimental needs. For example, our preliminary tests revealed that it was possible to prepare partially cleared samples for two-photon microscopy by using a low-stringency version of reagent 1 for several hours.

Rapid whole-brain imaging cannot deliver its maximum benefit without imaging devices optimized for the cleared tissues. Because LSFM showed potential for high-performance whole-brain imaging early in its development (Dodt et al., 2007), we optimized LSFM for lower spherical aberration (Figure S3A) and acquired 25 whole-brain images, most of which were collected within a few days. Our optimized LSFM setup could capture seamless whole-brain images with relatively high resolution. This is particularly important for comparing multiple 3D whole-brain images with single-cell resolution because the assembly of numerous plane images still has issues such as unavoidable errors of mechanical stage accuracy, the need for additional calculations to correct for optical distortion and rotation for reconstitution, or the accumulation of huge data sets (Emmenlauer et al., 2009; Preibisch et al., 2009). Improvements in illumination (Kalchmair et al., 2010; Leischner et al., 2009) and image processing (Mertz and Kim, 2010) and technological sharing through open

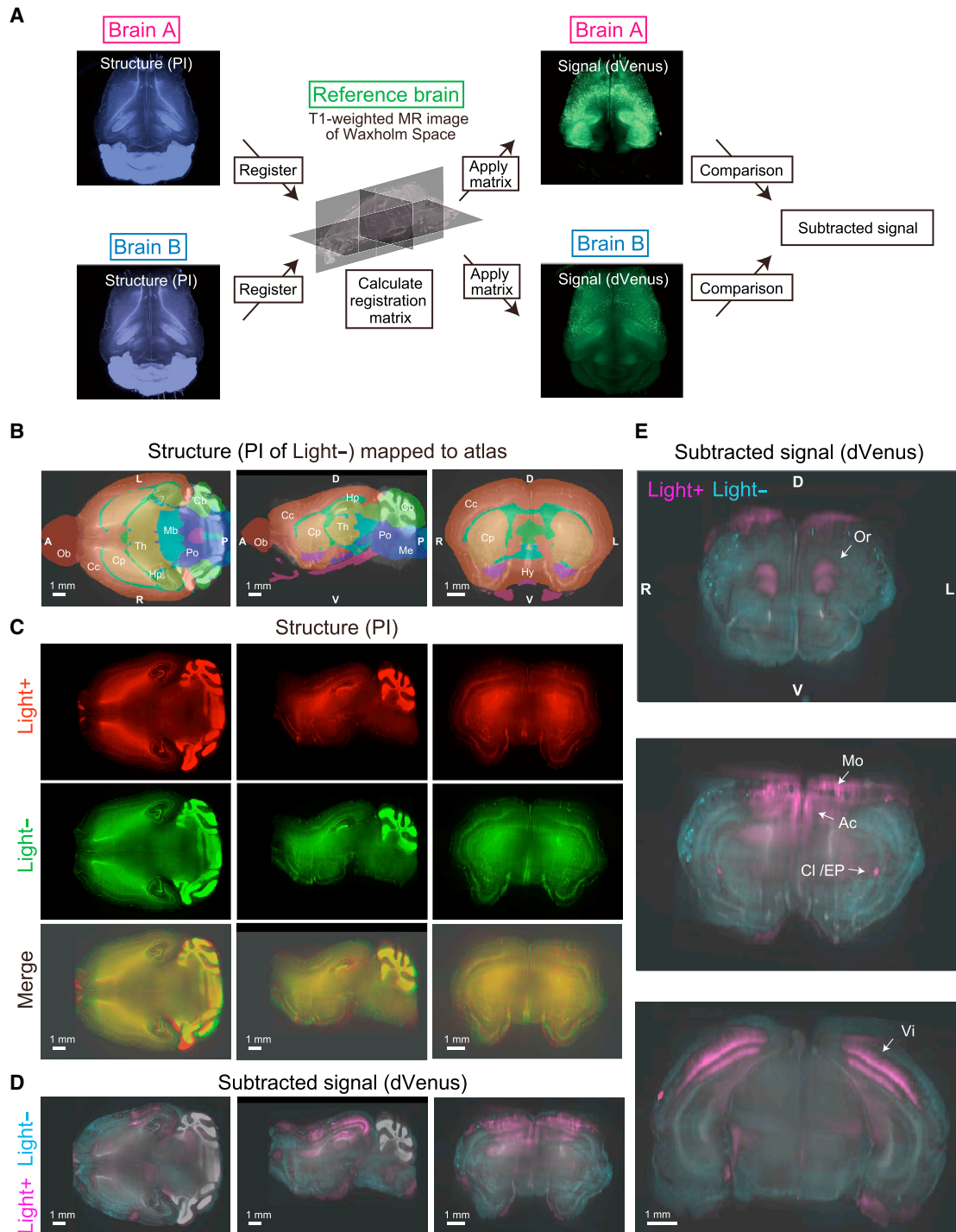


Figure 7. Computational Image Analysis Enables Gene Expression Profiling of Adult Whole Brains

(A) Scheme of CUBIC informatics pipeline (see Figure S7A). Structural information from a nuclear-stained image is used for registration to a reference brain so that a standardization matrix can be calculated. The resulting matrix is then applied to the corresponding signal image. Standardized images from different brains can be merged directly to generate a subtracted signal image.

(B) Standardized PI image mapped to the Waxholm Space atlas, after V-D and D-V image combination and standardization to the reference brain. The analysis was performed using downscaled NIFTI-1 files and visualized with ITK-SNAP (see Extended Experimental Procedures; also in C–E). Ob, olfactory bulb; Cc, cerebral cortex; Cp, caudoputamen; Hp, hippocampus; Th, thalamus; Mb, midbrain; Po, pons; Me, medulla; Cb, cerebellum; Hy, hypothalamus.

(C) PI images of two different brains (Light+ (1), red and Light–, green) and their overlays after V-D and D-V image combination, sample alignment, and standardization to the reference brain.

(legend continued on next page)

platforms such as OpenSPIM (Pitrone et al., 2013) will also advance the speed and resolution of whole-brain imaging. In addition, the development of an RI-adjusted objective lens will further facilitate the high-resolution imaging of CUBIC samples.

CUBIC Enables Whole-Brain Imaging with Single-Cell Resolution

In this study, we conducted whole-brain nuclear counterstaining using SYTO 16 or PI and successfully acquired structural information with anatomical annotation, which is important for whole-brain imaging with single-cell resolution (Figures 6B, 6C, and 7). Because CUBIC preserves global anatomical structure in brain specimens, the anatomical annotation was highly reproducible; for example, the PI images of two different brains in Light+ and Light− mice show substantial overlap (Figure 7C). In addition, the computationally standardized PI image mapped well to a “reference” brain such as that in the Waxholm Space atlas (Figure 7B), enabling reliable annotation of the observed signals. Imaging can be further improved by combining two whole-brain images of the same brain captured from opposite directions (D-V and V-D). Using an edge detection algorithm, it was possible to automatically define a weighted sum between images from these two directions and obtain a combined image that was sharp throughout the brain (Figures 7 and S7). This improved both the alignment to the reference structures and the clarity of the fluorescent signal images. The CUBIC protocol, together with CUBIC informatics, enabled the accurate comparison of multiple whole-brain images. This high-throughput method enables efficient handling of a large number of brain samples. This is particularly useful when investigating dynamic biological phenomena.

To realize system-level identification and analysis of cellular circuits in the brain, it will be important to combine high-throughput whole-brain imaging with other key technologies. One interesting synergy may exist with CRISPR/Cas-mediated genetically engineered mice, in which knockin animals harboring neural-activity reporters (e.g., Arc-dVenus) can be generated within a single generation (Yang et al., 2013). The comprehensive description of phenotype-correlated cells using such knockin mice is an important step in determining the cellular circuits underlying biological phenomena of interest. If neural activity modifiers such as tetanus toxin (Yamamoto et al., 2003), Allatostatin (Tan et al., 2006), or DREADDs and PSAMs (Armbruster et al., 2007; Magnus et al., 2011) could be selectively introduced and expressed in a limited population of cells together with a fluorescent protein marker, phenotype-responsive cells could be functionally identified by whole-brain imaging. The combination of neural activity modifiers (expressed in a limited neural population) and neural activity reporters (expressed throughout the brain) with CUBIC could

enable the identification and analysis of functional connectivity at the whole-brain level. In addition, anterograde and retrograde neural tracers, when used with the CUBIC protocol, could also provide direct connectivity information at the whole-brain level (Wickersham et al., 2007). When combined with other emerging technologies, CUBIC should contribute to the system-level identification and analysis of cellular circuits in the whole brain and probably in the whole body. New research fields such as whole-brain cell profiling or whole-body cell profiling (WBC profiling) lie ahead.

EXPERIMENTAL PROCEDURES

See [Extended Experimental Procedures](#) for additional details.

The CUBIC Protocol

ScaleCUBIC-1 (reagent 1) was prepared as a mixture of 25 wt% urea (Nacalai Tesque Inc., 35904-45, Japan), 25 wt% *N,N,N',N'*-tetrakis(2-hydroxypropyl) ethylenediamine (Tokyo Chemical Industry CO., LTD., T0781, Japan), and 15 wt% polyethylene glycol mono-*p*-isooctylphenyl ether/Triton X-100 (Nacalai Tesque Inc., 25987-85, Japan). ScaleCUBIC-2 (reagent 2) was prepared as a mixture of 50 wt% sucrose (Nacalai Tesque Inc., 30403-55, Japan), 25 wt% urea, 10 wt% 2,2',2''-nitrilotriethanol (Wako Pure Chemical Industries Ltd., 145-05605, Japan), and 0.1% (v/v) Triton X-100. For whole-brain clearing, each fixed brain was immersed in 10 g of reagent 1 at 37°C with gentle shaking for 3 days, after which the solution was exchanged and the sample immersed in the same volume of fresh reagent 1 for an additional 3–4 days. The treated brain was washed with PBS several times at room temperature while gently shaking, immersed in 20% (w/v) sucrose in PBS, degassed, and immersed in reagent 2 (10 g per brain) for 3–7 days. After imaging, the sample was again washed with PBS, immersed in 20% (w/v) sucrose in PBS, and stored in O.C.T. compound at −80°C.

Microscopy

Whole-brain fluorescence images were acquired with an LSMF (Ultramicroscope, LaVision BioTec, Germany) using 488 and 588 nm lasers, an sCMOS camera, and a macrozoom microscope (Figure S3A). Each plane was illuminated from both the right and left sides of the sample, and a merged image was saved. Immunostained SCN and cerebral cortex images were acquired with an inverted confocal microscope (Leica TCS SP8 or Carl Zeiss LSM700). Images of Arc-dVenus Tg brains (Figure S6A) were captured with a fluorescence stereomicroscope using the same settings as previously described (Eguchi and Yamaguchi, 2009). Two-photon imaging was performed using an upright multiphoton microscope (Olympus FV1000, BX61WI or Carl Zeiss LSM7MP).

Image Data Processing and the CUBIC Informatics

All raw imaging data were collected in a lossless TIFF format. 3D-rendered images were visualized and captured with Imaris software (Version 7.6.4, Bitplane). 3D brain images in the NIFTI-1 format are constructed with Convert3D from ITK-SNAP (Yushkevich et al., 2006). The combination of two images acquired from opposite directions into a single composite 3D image ensured the optimal sharpness of the 3D brain images. The reference atlas used in our analysis was the Waxholm Space Atlas (Johnson et al., 2010). To facilitate analysis across samples, whole-brain images were registered and aligned to reference structures. We aligned images by pairs, in which one image corresponded to the structural information (obtained via nuclear staining) and the other to the fluorescent signal

(D) Subtraction data of Light+ (1) and Light− dVenus images, corresponding to sections in (B) and (C).

(E) Subtraction data of Light+ (1) and Light− dVenus images, corresponding to coronal images in Figures 6B and 6C. Pink and light blue indicate regions where the Venus signals were stronger under Light+ and Light− conditions, respectively. Areas where Venus signals were increased in the Light+ brain are indicated as in Figure 6B. In (D) and (E), images were overlaid with the PI data of Light+ (1) specimen.

See also Figure S7.

channel. Thus, the analysis of each pair required two steps: (1) registration of the structural information to a reference and (2) alignment of both images by applying the transformation (calculated during registration) to both the structural image and the fluorescent image (Figure 7A). For image registration, we used advanced normalization tools (ANTs), which have proved successful in resolving a number of image registration issues (Murphy et al., 2011).

SUPPLEMENTAL INFORMATION

Supplemental Information includes Extended Experimental Procedures, seven figures, one table, and seven movies and can be found with this article online at <http://dx.doi.org/10.1016/j.cell.2014.03.042>.

AUTHOR CONTRIBUTIONS

H.R.U., E.A.S., K.T., and D.P. designed the study. E.A.S. performed most of the biological experiments. K.T. performed chemical screening. D.P. performed most of the computational image analysis. F.K. contributed to the chemical screening. T.T. and H.Y. contributed to the computational image analysis. T.M.W. settled the LSMF imaging system. C.Y. and H.O. housed marmosets and prepared marmoset brains. M.E. and S.Y. prepared Arc-Venus brains. T.A. and H.K. produced R26-H2B-mCherry and -EGFP mice. Y.S. produced recombinant fluorescent proteins. A.M. provided details on previous brain-clearing methods. All authors discussed the results and commented on the manuscript text.

ACKNOWLEDGMENTS

We thank the lab members at RIKEN CDB and QBiC, in particular, S. Hirahara, J. Hara, H. Ukai, N. Koide, J. Yoshida, C. Imai, and Y. Niwa for their kind help in preparing the materials and C. Jolley for helpful advice. We also thank T. Imai for sharing the SeeDB protocol before its publication, H. Hama for testing Scale protocol with our samples before its publication, H. Niwa for providing a vector with a CAG promoter, H. Sekiya for supporting two-photon imaging experiments, the LARGE, RIKEN CDB for housing the mice, Emi Kosano for illustrating the mouse in Figure 6, and Olympus and Olympus Engineering for optimizing the Ultramicroscope setup. This work was supported by the Program for Innovative Cell Biology by Innovative Technology from the Ministry of Education, Culture, Sports, Science and Technology (MEXT) of Japan, a Grant-in-Aid for Scientific Research (S) (Grant No. 25221004) and a Grant-in-Aid for Scientific Research on Innovative Areas (Grant No. 23115006) from MEXT/Japan Society for the Promotion of Science (JSPS), the strategic programs for R&D (President's discretionary fund) of RIKEN, an intramural Grant-in-Aid from the RIKEN Center for Developmental Biology and RIKEN Quantitative Biology Center, a grant from Core Research for Evolutional Science and Technology (CREST) and Precursory Research for Embryonic Science and Technology (PRESTO) of Japan Science and Technology Agency (JST), the RIKEN Special Postdoctoral Research Program, a Grant-in-Aid from Japan Foundation for Applied Enzymology, a Grant-in-Aid from the Shimabara Science Promotion Foundation, and by the RIKEN Foreign Postdoctoral Researcher Program.

Received: January 20, 2014

Revised: March 3, 2014

Accepted: March 27, 2014

Published: April 17, 2014

REFERENCES

Abe, T., Kiyonari, H., Shioi, G., Inoue, K.I., Nakao, K., Aizawa, S., and Fujimori, T. (2011). Establishment of conditional reporter mouse lines at ROSA26 locus for live cell imaging. *Genesis* 49, 579–590.

Abrahamson, E.E., and Moore, R.Y. (2001). Suprachiasmatic nucleus in the mouse: retinal innervation, intrinsic organization and efferent projections. *Brain Res.* 916, 172–191.

Armbruster, B.N., Li, X., Pausch, M.H., Herlitze, S., and Roth, B.L. (2007). Evolving the lock to fit the key to create a family of G protein-coupled receptors potentially activated by an inert ligand. *Proc. Natl. Acad. Sci. USA* 104, 5163–5168.

Avants, B.B., Tustison, N.J., Song, G., Cook, P.A., Klein, A., and Gee, J.C. (2011). A reproducible evaluation of ANTs similarity metric performance in brain image registration. *Neuroimage* 54, 2033–2044.

Becker, K., Jährling, N., Saghafi, S., Weiler, R., and Dodt, H.U. (2012). Chemical clearing and dehydration of GFP expressing mouse brains. *PLoS ONE* 7, e33916.

Chudakov, D.M., Matz, M.V., Lukyanov, S., and Lukyanov, K.A. (2010). Fluorescent proteins and their applications in imaging living cells and tissues. *Physiol. Rev.* 90, 1103–1163.

Chung, K., Wallace, J., Kim, S.Y., Kalyanasundaram, S., Andalman, A.S., Davidson, T.J., Mirzabekov, J.J., Zalocusky, K.A., Mattis, J., Denisin, A.K., et al. (2013). Structural and molecular interrogation of intact biological systems. *Nature* 497, 332–337.

Cormack, A.M. (1973). Reconstruction of densities from their projections, with applications in radiological physics. *Phys. Med. Biol.* 18, 195–207.

Dodt, H.U., Leischner, U., Schierloh, A., Jährling, N., Mauch, C.P., Deininger, K., Deussing, J.M., Eder, M., Ziegglänsberger, W., and Becker, K. (2007). Ultramicroscopy: three-dimensional visualization of neuronal networks in the whole mouse brain. *Nat. Methods* 4, 331–336.

Eguchi, M., and Yamaguchi, S. (2009). *In vivo* and *in vitro* visualization of gene expression dynamics over extensive areas of the brain. *Neuroimage* 44, 1274–1283.

Emmenlauer, M., Ronneberger, O., Ponti, A., Schwarb, P., Griffla, A., Filippi, A., Nitschke, R., Driever, W., and Burkhardt, H. (2009). XuvTools: free, fast and reliable stitching of large 3D datasets. *J. Microsc.* 233, 42–60.

Ertürk, A., Becker, K., Jährling, N., Mauch, C.P., Hojer, C.D., Egen, J.G., Hellal, F., Bradke, F., Sheng, M., and Dodt, H.U. (2012). Three-dimensional imaging of solvent-cleared organs using 3DISCO. *Nat. Protoc.* 7, 1983–1995.

Feng, G.P., Mellor, R.H., Bernstein, M., Keller-Peck, C., Nguyen, Q.T., Wallace, M., Nerbonne, J.M., Lichtman, J.W., and Sanes, J.R. (2000). Imaging neuronal subsets in transgenic mice expressing multiple spectral variants of GFP. *Neuron* 28, 41–51.

Gong, H., Zeng, S.Q., Yan, C., Lv, X.H., Yang, Z.Q., Xu, T.H., Feng, Z., Ding, W.X., Qi, X.L., Li, A.A., et al. (2013). Continuously tracing brain-wide long-distance axonal projections in mice at a one-micron voxel resolution. *Neuroimage* 74, 87–98.

Hägerling, R., Pollmann, C., Andreas, M., Schmidt, C., Nurmi, H., Adams, R.H., Alitalo, K., Andresen, V., Schulte-Merker, S., and Kiefer, F. (2013). A novel multistep mechanism for initial lymphangiogenesis in mouse embryos based on ultramicroscopy. *EMBO J.* 32, 629–644.

Hama, H., Kurokawa, H., Kawano, H., Ando, R., Shimogori, T., Noda, H., Fukami, K., Sakaue-Sawano, A., and Miyawaki, A. (2011). Scale: a chemical approach for fluorescence imaging and reconstruction of transparent mouse brain. *Nat. Neurosci.* 14, 1481–1488.

Johnson, G.A., Badea, A., Brandenburg, J., Cofer, G., Fubara, B., Liu, S., and Nissanov, J. (2010). Waxholm space: an image-based reference for coordinating mouse brain research. *Neuroimage* 53, 365–372.

Kalchmair, S., Jährling, N., Becker, K., and Dodt, H.U. (2010). Image contrast enhancement in confocal ultramicroscopy. *Opt. Lett.* 35, 79–81.

Ke, M.T., Fujimoto, S., and Imai, T. (2013). SeeDB: a simple and morphology-preserving optical clearing agent for neuronal circuit reconstruction. *Nat. Neurosci.* 16, 1154–1161.

Kitano, H. (2002). Systems biology: a brief overview. *Science* 295, 1662–1664.

Kneen, M., Farinas, J., Li, Y.X., and Verkman, A.S. (1998). Green fluorescent protein as a noninvasive intracellular pH indicator. *Biophys. J.* 74, 1591–1599.

Land, H., Schütz, G., Schmale, H., and Richter, D. (1982). Nucleotide sequence of cloned cDNA encoding bovine arginine vasopressin-neurophysin II precursor. *Nature* 295, 299–303.

- Lauterbur, P.C. (1973). Image formation by induced local interactions: Examples employing nuclear magnetic resonance. *Nature* 242, 190–191.
- Leischner, U., Zieglgänsberger, W., and Dodt, H.U. (2009). Resolution of ultra-microscopy and field of view analysis. *PLoS ONE* 4, e5785.
- Li, A.A., Gong, H., Zhang, B., Wang, Q.D., Yan, C., Wu, J.P., Liu, Q.A., Zeng, S.Q., and Luo, Q.M. (2010). Micro-optical sectioning tomography to obtain a high-resolution atlas of the mouse brain. *Science* 330, 1404–1408.
- Magnus, C.J., Lee, P.H., Atasoy, D., Su, H.H., Looger, L.L., and Sternson, S.M. (2011). Chemical and genetic engineering of selective ion channel-ligand interactions. *Science* 333, 1292–1296.
- Mertz, J., and Kim, J. (2010). Scanning light-sheet microscopy in the whole mouse brain with HiLo background rejection. *J. Biomed. Opt.* 15, 016027.
- Miller, M.W., and Vogt, B.A. (1984). Direct connections of rat visual cortex with sensory, motor, and association cortices. *J. Comp. Neurol.* 226, 184–202.
- Murphy, K., van Ginneken, B., Reinhardt, J.M., Kabus, S., Ding, K., Deng, X., Cao, K., Du, K., Christensen, G.E., Garcia, V., et al. (2011). Evaluation of registration methods on thoracic CT: the EMPIRE10 challenge. *IEEE Trans. Med. Imaging* 30, 1901–1920.
- Navone, F., Greengard, P., and De Camilli, P. (1984). Synapsin I in nerve terminals: selective association with small synaptic vesicles. *Science* 226, 1209–1211.
- Niwa, H., Yamamura, K., and Miyazaki, J. (1991). Efficient selection for high-expression transfectants with a novel eukaryotic vector. *Gene* 108, 193–199.
- Ogawa, S., Lee, T.M., Nayak, A.S., and Glynn, P. (1990). Oxygenation-sensitive contrast in magnetic resonance image of rodent brain at high magnetic fields. *Magn. Reson. Med.* 14, 68–78.
- Pitrone, P.G., Schindelin, J., Stuyvenberg, L., Preibisch, S., Weber, M., Eliceiri, K.W., Huisken, J., and Tomancak, P. (2013). OpenSPIM: an open-access light-sheet microscopy platform. *Nat. Methods* 10, 598–599.
- Preibisch, S., Saalfeld, S., and Tomancak, P. (2009). Globally optimal stitching of tiled 3D microscopic image acquisitions. *Bioinformatics* 25, 1463–1465.
- Reep, R.L., Corwin, J.V., and King, V. (1996). Neuronal connections of orbital cortex in rats: topography of cortical and thalamic afferents. *Exp. Brain Res.* 111, 215–232.
- Sasaki, E., Suemizu, H., Shimada, A., Hanazawa, K., Oiwa, R., Kamioka, M., Tomioka, I., Sotomaru, Y., Hirakawa, R., Eto, T., et al. (2009). Generation of transgenic non-human primates with germline transmission. *Nature* 459, 523–527.
- Sloniewski, P., Usunoff, K.G., and Pilgrim, C. (1986). Retrograde transport of fluorescent tracers reveals extensive ipsi- and contralateral claustricortical connections in the rat. *J. Comp. Neurol.* 246, 467–477.
- Tan, E.M., Yamaguchi, Y., Horwitz, G.D., Gosgnach, S., Lein, E.S., Goulding, M., Albright, T.D., and Callaway, E.M. (2006). Selective and quickly reversible inactivation of mammalian neurons *in vivo* using the *Drosophila* allatostatin receptor. *Neuron* 51, 157–170.
- Tomer, R., Khairy, K., and Keller, P.J. (2011). Shedding light on the system: studying embryonic development with light sheet microscopy. *Curr. Opin. Genet. Dev.* 21, 558–565.
- van der Horst, G.T.J., Muijtjens, M., Kobayashi, K., Takano, R., Kanno, S., Takao, M., de Wit, J., Verkerk, A., Eker, A.P.M., van Leenen, D., et al. (1999). Mammalian *Cry1* and *Cry2* are essential for maintenance of circadian rhythms. *Nature* 398, 627–630.
- Wickersham, I.R., Finke, S., Conzelmann, K.K., and Callaway, E.M. (2007). Retrograde neuronal tracing with a deletion-mutant rabies virus. *Nat. Methods* 4, 47–49.
- Yamamoto, M., Wada, N., Kitabatake, Y., Watanabe, D., Anzai, M., Yokoyama, M., Teranishi, Y., and Nakanishi, S. (2003). Reversible suppression of glutamatergic neurotransmission of cerebellar granule cells *in vivo* by genetically manipulated expression of tetanus neurotoxin light chain. *J. Neurosci.* 23, 6759–6767.
- Yang, H., Wang, H.Y., Shivalila, C.S., Cheng, A.W., Shi, L.Y., and Jaenisch, R. (2013). One-step generation of mice carrying reporter and conditional alleles by CRISPR/Cas-mediated genome engineering. *Cell* 154, 1370–1379.
- Yushkevich, P.A., Piven, J., Hazlett, H.C., Smith, R.G., Ho, S., Gee, J.C., and Gerig, G. (2006). User-guided 3D active contour segmentation of anatomical structures: significantly improved efficiency and reliability. *Neuroimage* 31, 1116–1128.

EXTENDED EXPERIMENTAL PROCEDURES

Mice

The R26-pCAG-nuc-3 × mKate2 knockin mouse strain was established in our laboratory. A vector harboring all of the required elements, including the CAG promoter from pPyCAG-BstXI-IP (Niwa et al., 1991), the cDNAs encoding the nuclear localization signal of the SV40 Large T-antigen (PKKKRKV) and the triplicated mKate2 from pmKate2-C (Evrogen), the woodchuck hepatitis post-transcriptional regulatory element (WPRE) from pTRIPZ (Thermo Scientific Open Biosystems), and the bovine growth hormone polyA sequence from pPyCAG-BstXI-IP, was constructed by inserting these sequences at the Sall and NotI sites of pENTR-1A (Invitrogen). In addition the Puro-resistance gene cassette (pPGK-PuroR-poly A) flanked by FRT sequences was inserted at the EcoRV site of the vector. The resulting expression vector (pENTR-1A_CAG-nuc-3 × mKate2-WPRE-PuroR) was then mixed with the ROSA26 targeting vector (Abe et al., 2011), which contains the Reading Frame Cassette B from the Gateway Conversion System (Invitrogen) at the blunted KpnI and Ascl sites, to perform the LR recombination reaction using the Gateway system. In the resulting targeting vector, the insertion cassette was in the same orientation as the ROSA26 gene. The targeting vector was purified and introduced into HK3i C57BL/6 mouse embryonic stem (ES) cells as described previously (Kiyonari et al., 2010) with some modification, and the homologous recombined, puro-resistant ES cell clones were isolated for further culture and expansion. An aliquot of the cells was lysed and screened for successful homologous recombination by PCR. The integrity of the targeted region was confirmed by PCR using primers annealing outside the homologous recombination arms and within the inserted cassette. The primers used for the screening and the confirmation of genome integrity were as follows: 1) forward primer annealing to the region upstream of the 5' homologous arm: 5'-TGCTGGCCTACTGCTGCCTCGATCTTAC-3', 2) reverse primer annealing to the region downstream of the 5' homologous arm: 5'-AGGACAACGCCACACACCAGGTTAGC-3', 3) forward primer annealing to the region upstream of the 3' homologous arm: 5'-CGTGGTGGAGCCGTTCTGTGAGACA-3', 4) reverse primer annealing to the region downstream of the 3' homologous arm: 5'-GGTGAAATGCTTGACTCCTAGACTT-3', 5) reverse primer annealing to the CAG promoter: 5'-CAGCCAGCGGGCCATTACCGTAAGTTAT-3', and 6) forward primer annealing to the poly-A region of the puro-resistance gene: 5'-TCCATCAGAAGCTGGTCGATC-3'. The copy number of the inserted cassette was confirmed with a quantitative PCR assay using primers annealing to the coding sequences of the puro-resistance gene (forward primer: 5'-CTCGACATCGGCAAGGTGTG-3', reverse primer: 5'-GGCCTTCCATCTGTTGCTGC-3'), normalized to the amount of TATA-box binding protein gene amplification (forward primer: 5'-CCCCCTCTGCACGAAATCA-3', reverse primer: 5'-GTAGCAGCACAGAGCAAGCAA-3') (Tsuji no et al., 2013) using the SYBR Premix Ex Taq GC (Takara #RR071A) and the ABI PRISM 7900 (Applied Biosystems). The selected ES cell clones were injected into 8-cell-stage ICR embryos to generate ~100% ES cell-derived chimeras (Kiyonari et al., 2010).

We also used the R26-H2B-EGFP (CDB0238K) and R26-H2B-mCherry (CDB0239K) mouse strains (http://www.cdb.riken.jp/arg/reporter_mice.html) (Abe et al., 2011) and the Thy1-YFP-H transgenic mouse strain (Feng et al., 2000) to observe static fluorescent gene-expression patterns in whole-brain imaging (Figure 3, S3, S5 and S7).

For the SCN immunostaining assay (Figure 4 and S4), R26-H2B-EGFP knockin mice housed under 12 h:12 hr light-dark conditions were sacrificed for fixation at ZT0 and ZT12. C57BL/6 wild-type mice or *Cry1^{-/-}*, *Cry2^{-/-}* mice (van der Horst et al., 1999) were adapted to light-dark conditions for over 2 weeks followed by maintenance under constant dark (DD) conditions. The sampling was performed after 24 hr of exposure (CT12 of day-0 to CT12 of day-1) to DD conditions, at CT12 and 18 of day-1, and at CT0 and 6 of day-2. Samples were obtained from multiple animals within 30 min.

To obtain fixed brains from these mice, each animal was anesthetized with an overdose of pentobarbital (>100 mg/kg, i. p.; Somnopentyl, Kyoritsu Seiyaku, Japan). The subject was transcardially perfused with PBS containing ~10 U/mL of heparin (Wako Pure Chemical Industries, Japan) to flush the blood vessels and followed by perfusion with 4% (w/v) paraformaldehyde (PFA) in PBS (pH 7.4) for fixation. The acrylamide-embedded brain sample of CLARITY protocol was prepared as described previously (Chung et al., 2013).

The Arc-dVenus transgenic mice (line D) (Eguchi and Yamaguchi, 2009) were housed under DD conditions for about 2.5 days followed by 1500 lux of white light stimulation from CT2.5. After 5 hr of the stimulation, the mice were sacrificed for fixation together with an unstimulated animal (Figure 6A). We conducted the light stimulation and sampling of multiple animals within ± 30 min. For sampling, the mice were deeply anesthetized with ether. Then, the subject was transcardially perfused with PBS containing 5 U/mL of heparin (Wako Pure Chemical Industries, Japan) to flush the blood vessels and followed by perfusion with 4% (w/v) PFA in 0.1 M PB (pH 7.4) for fixation.

Each excised brain was postfixed with the same fixation solution for 18 to 24 hr at 4°C. The fixed brain was immersed in 20% (w/v) sucrose in PBS at 4°C to remove PFA and for the following cryopreservation. If necessary, the sample was stocked in O.C.T. compound (Sakura Finetek, Japan) at -80°C until use. When the frozen sample was used for CUBIC protocol, it was thawed and washed with PBS and then immersed in CUBIC reagents. Note that the freezing step is merely for stocking samples and not compulsory.

All experimental procedures and housing conditions were approved by the Animal Care and Use Committee of the RIKEN Kobe Institute or by the Gifu University Animal Experiment Committee, and all of the animals were cared for and treated humanely in accordance with the Institutional Guidelines for Experiments using animals. All mouse strains were maintained by crossing onto a C57BL/6 background.

Marmoset

We studied a newborn infant marmoset at the age of three days, an offspring of a breeding pair aged three and four years. The animals were housed in home cages measuring 1670 × 610 × 620 mm under 12 h:12 hr light-dark conditions (light: 08:00–20:00). Each cage had four wooden perches, a food tray, and an automatic water dispenser. Animals were fed twice a day with solid food (CMS-1, CLEA Japan, Tokyo, Japan) soaked in water, mixed with suitable amounts of powdered milk formula, honey, gluconic acid calcium, vitamin C, and lactobacillus probiotic. In addition, their diet was supplemented with chopped boiled eggs or bananas once a week. Water was provided ad libitum. For fixed brain sampling, the three-day-old marmoset was anesthetized with an overdose of pentobarbital (40 mg/kg, i.p.; Somnopentyl, Kyoritsu Seiyaku, Japan) after an intramuscular injection of ketamine (30 mg/kg; Ketalar, Daiichi Sankyo Propharma, Japan). The subject was transcardially perfused with PBS containing ~10 U/mL heparin (Wako Pure Chemical Industries, Japan) to flush the blood vessels and followed by perfusion with 4% (w/v) PFA in PBS (pH 7.4) for fixation. The excised brain was postfixed with the same solution for 18 to 24 hr at 4°C. The fixed brain was immersed in 20% (w/v) sucrose in PBS at 4°C and finally stocked in O.C.T. compound (Sakura Finetek, Japan) at –80°C until use. Animals were maintained and handled in accordance with the recommendations of the United States National Institutes of Health, and all procedures were approved by the Animal Care and Use Committee of the RIKEN Kobe Institute.

Chemical Screening

The usage of one fixed whole brain per one chemical compound (or one chemical configuration) is not desirable for first chemical screening because it is time-consuming, labor-intensive and even unethical to prepare numbers of fixed mouse brains to test many chemical configurations. Therefore, we developed a new evaluation protocol, in which we exchanged the order of fixation and isolation, and also introduced homogenization processes (chopping and sonication) in order to test many chemical configurations using only one mouse brain. An adult mouse brain was removed from the skull, chopped with a blade, suspended and sonicated in PBS, and gradually mixed with the same volume of 8% (w/v) PFA in PBS (pH 7.4). The resulting fixed brain suspension was washed with PBS several times and finally used for the solubilization assay in Figure 1A and 1B to evaluate the clearing efficiency of each cocktail. The suspension was centrifuged to remove PBS, and resuspended in candidate chemical solutions (10 wt% in water) followed by 24 hr of incubation at room temperature. The OD600 of the incubated mixture was measured with the PowerWave XS and the attached operation software (Bio-Tek). The relative OD600s were calculated by fitting to a standard curve generated by diluting several concentrated mixtures of the suspension in PBS. The relative transmittance value of each sample (defined as 100% minus the relative OD600) was qualitatively consistent with the expected brain-clearing capability (Figure 1A, graph of the right panel). The chemical solutions were also mixed with recombinant EGFP (0.1 mg/mL, final concentration) and incubated for 12 hr at room temperature, and the resulting fluorescent signals were measured with the ARVO MX (PerkinElmer, USA). The values of the chemical solutions (without the fluorescent protein) were also measured and subtracted as the background signal. Relative fluorescence was calculated by normalization with an EGFP sample that was mixed and incubated with PBS, and titrated to show linearity. All data were calculated as an average of duplicated measurements, and two independent experiments were performed (Figure 1B and C). The chemicals were also assayed for their effects on the fluorescence of EYFP, mCherry (0.1 mg/mL, final concentration) and mKate2 (0.05 mg/mL, final concentration) in addition to EGFP in Figure 2C, but are shown as raw fluorescent values. To prepare the recombinant fluorescent proteins, the genes encoding them (containing a His-tag at the N terminus) were cloned into pET15b (Merck Millipore) and transformed into the *E. coli* BL21/DE3 strain. Overexpressed proteins were purified with Ni-NTA agarose (QIAGEN) according to the manufacturer's instructions. The refractive indices of the solutions in the chemical screening were measured by an Abbe refractometer (ATAGO, DR-A1, Japan).

We have developed improved brain tissue clearing reagents by comprehensive chemical screening described above. During the screening process, we followed the principle that brain clearing reagents should be developed that: a) minimize light scattering in the sample by adjusting the inner RI to approximately 1.5, and b) preserve the signals from fluorescent proteins and antibodies to visualize functional activities and obtain structural information. Since hydrophobic lipids are a major source of light scattering in the fixed brain, the adjustment of RIs using hydrophobic reagents has traditionally been used to transparentize the brain. The classic BABB protocol involves an initial dehydration step with ethanol followed by an RI-adjustment step with benzyl alcohol:benzyl benzoate (1:2 ratio), resulting in transparent brain specimens. However, both steps suppress EGFP fluorescence (Hama et al., 2011). Among hydrophobic organic chemicals, the use of THF as a dehydrant and DBE as an RI-adjusting medium increased the preservation of EGFP fluorescence with improved tissue transparency (Becker et al., 2012). However, EYFP fluorescence was still significantly quenched by DBE (Ertürk et al., 2012; Ke et al., 2013). Thus, it may be intrinsically difficult for hydrophobic media to provide efficient clearing with fluorescence signal preservation. In contrast, Sca/e was developed based on water-soluble clearing reagents (Hama et al., 2011). Sca/e contains kosmotropic glycerol (which stabilizes intermolecular interactions) and chaotropic urea (which disturbs hydrogen networks) as hydration-promoting agents. Since Sca/e promotes the optical clearing of brain specimens despite its relatively low RI (1.38), the chemicals in Sca/e may permeate the brain tissue efficiently. Sca/e also preserves the signals of fluorescent proteins. The original Sca/e protocol (e.g., Sca/eA2) is suitable for clearing fetal mouse brains, but has drawbacks such as a long incubation time and sample swelling (Ke et al., 2013). Another hydrophilic clearing reagent, SeeDB, a highly concentrated fructose aqueous solution that functions as an RI-adjusting medium, overcomes these issues (Ke et al., 2013). Brain specimens treated with SeeDB are transparentized within a few days, and do not show sample expansion. These features are

partly due to SeeDB's high RI and osmotic pressure, which leads to the exclusion of water molecules and the permeation of fructose molecules. However, highly myelinated adult brain samples treated with these hydrophilic reagents were not sufficiently transparent for observation using rapid whole-brain imaging with LSM. Thus, while the hydration-promoting and hydrophilic clearing reagents were effective in some cases, improvements were needed to increase their applicability. Although it may be difficult to promote dehydration with water-soluble chemicals, the simultaneous improvements in dehydration and RI homogenization by a highly osmotic and RI-aqueous medium like SeeDB was a promising approach. Based on these previous findings, we sought to develop a simple and efficient tissue-clearing protocol.

We used a comprehensive chemical screening approach to gain insight into the chemical mechanisms that contribute to effective clearing. Our improved strategy reduced the number of mice required and facilitated the quantitative evaluation of a reagent's clearing ability by measuring the transparency of a homogenized suspension instead of a whole brain. Although polyhydric alcohols including glycerol have traditionally been used, their clearing ability against hydrophobic lipids and proteins had not been quantitatively evaluated. Unexpectedly, #18 glycerol and other hydrocarbon polyols [except #11 1,4-bis(2-hydroxyethoxy)-2-butynol] did not cause a significant increase in the transparency of brain suspension in our experiment (Figure 1B). In contrast, our screening revealed that a series of aminoalcohols transparentized the suspension quite efficiently. Positively charged amino groups may contribute to the neutralization of negatively charged phospholipids, which are the most abundant lipids in the brain (Morell and Quarles, 1999). As expected, all of the tested detergents were relatively effective in clearing the suspension. Among them, the nonionic detergents (except for a specific Triton X-100) quenched the EGFP fluorescence (Figure 1C). Deoxycholate was the best candidate for clearing detergents in the first screening, but led to EGFP quenching in the presence of aminoalcohol and urea. Chaotropic agents such as urea are well-known surfactants that disrupt noncovalent interactions such as protein-protein, protein-lipid, and lipid-lipid associations. Urea has been shown to clear brain tissue effectively (Hama et al., 2011), although the chemical mechanism is poorly understood. We further investigated the clearing ability of urea-related chemicals such as aprotic solvents without amide, urea-like amides, and other chaotropic agents. Aprotic solvents without amide (#31 acetonitrile, #39 dimethylsulfoxide, and #40 1,4-dioxane) and urea-like amides (#29 *N,N*-dimethylacetamide and #30 *N,N*-dimethylformamide) did not significantly clear the suspension. Other urea-like amides (#32 oxamide, #34 *N*-carboxymethylurea, and #37 biuret) were difficult to dissolve in water. Among the chaotropic agents, #38 thiourea caused higher transparency than #36 urea, while #33 guanidine hydrochloride did not clear the suspension. Our chemical screenings in this study and the previous work on *Scale* indicated that urea's chemical structure and chaotropic ability would contribute to the efficient clearing of brain tissues. Taking into account the heterogeneity of the biochemical components in the brain, we prepared reagent 1, which consisted of aminoalcohol, Triton X-100 and urea, analogous to the components in *ScaleA2* reagents (Figure S1B). Another urea-like molecule, formamide, can be also used for tissue-clearing as indicated in the recent study (*Clear^T*) (Kuwajima et al., 2013). Comparison between urea and formamide in the CUBIC protocol will be a subject of future investigation.

Reagent 1 treatment of the whole mouse brain resulted in a highly transparent sample (Figure 2A). The lipid-rich white matter was not completely cleared, however, suggesting that lipid removal was incomplete and that the RIs of the reagent and the sample were imperfectly matched. We sought to identify additional reagents that might increase brain tissue transparency through RI adjustment. As a solute's concentration increases, the osmotic pressure and RI increase simultaneously. Thus, large water-soluble molecules such as sugars are excellent candidates for solutes that will yield high-RI solutions. Fructose is one of the most water-soluble solutes, but aminoalcohols obtained from our screening would react with the aldehyde group of fructose, resulting in a brownish color via the Maillard reaction. Thus, sucrose was selected instead. Previous studies used a 60% sucrose aqueous solution for brain clearing (Tsai et al., 2009), but the clearing efficiency was much lower than for *Scale* or SeeDB (Hama et al., 2011; Ke et al., 2013). We prepared a highly osmotic, high-RI solution, reagent 2 (RI = 1.48-1.49), by mixing concentrated sucrose with cocktails based on the reagent 1 composition. When reagent-1-treated brain samples were then subjected to reagent 2, deeper regions of the brain, including the dense lipidic myelin sheath were transparentized (Figure 2A). In addition, sample swelling was minimized because the permeation of chemicals into the tissue was balanced by osmotic dehydration during reagent 2 treatment. The combination of reagent 1, *Scale*-inspired chemicals that promote tissue permeation, and reagent 2, a highly osmotic, high-RI aqueous reagent that promotes RI-homogenizing dehydration, resulted in improved clearing of the adult mouse whole brain without denaturing fluorescent proteins and antibodies.

Measurement of Light Transmittance

Brain sample transmittance was measured with the CM-5 spectrophotometer (Konica-Minolta, Japan). For this, 100% transmittance was calibrated with a 5×10 mm slit, and samples were placed on a 5×2 mm slit for measurement. The blank value was measured as the transmittance of the latter slit without the dish and sample. Each value was determined as an average of duplicate measurements. The ventral-to-dorsal transmittance of the central part of the whole brain immersed in the indicated reagents was measured for Figure 2B. The central-to-lateral transmittance of the thickest part of a hemisphere placed on a plastic bottom dish without liquid was measured for Figure 1E and S1A, to make the procedure easier and avoid difficulties cementing samples to the dish. As a result, some of the measured values exceeded 100%, which we speculate is a consequence of the hemisphere acting as a convex lens because of the mismatch in RI between the air and the CUBIC samples. In this case, the values are notated as relative values (A.U.) rather than % transmittance.

The CUBIC Protocol

ScaleCUBIC-1 (reagent 1) was prepared as a mixture of 25 wt% urea (Nacalai Tesque, 35904-45, Japan), 25 wt% *N,N,N',N'*-tetrakis(2-hydroxypropyl)ethylenediamine (Tokyo Chemical Industry CO., LTD., T0781, Japan), and 15 wt% polyethylene glycol mono-*p*-isooctylphenyl ether/Triton X-100 (Nacalai Tesque, 25987-85, Japan). Some technical tips regarding reagent 1 preparation are as follows: 1) *N,N,N',N'*-tetrakis(2-hydroxypropyl)ethylenediamine is a highly viscous liquid and can be used as an 80 wt% working solution. 2) The quality of Triton X-100 product seems critical for preserving fluorescent signals and we highly recommend the product indicated above. When the same chemical from other vendors is used, the quenching effect on recombinant fluorescent proteins should be checked. ScaleCUBIC-2 (reagent 2) was prepared as a mixture of 50 wt% sucrose (Nacalai Tesque Inc., 30403-55, Japan), 25 wt% urea, 10 wt% 2,2',2''-nitrioltriethanol (Wako Pure Chemical Industries, 145-05605, Japan), and 0.1% (v/v) Triton X-100. We referred the concentration of urea in ScaleA2 (4 M) (Hama et al., 2011), for determining its concentration in CUBIC reagents (25 wt%). Other components were added as much as possible, considering fluorescent signals and viscosity. Both reagent 1 and 2 were prepared just prior to use. When mixed, a hot stirrer should be used except during the addition of Triton X-100. Because water evaporation will make it difficult for the highly concentrated chemicals to dissolve, the weight should be monitored frequently for the addition of evaporated water during the mixing step. After confirming that all the mixed chemicals are dissolved, the reagents are cooled to room temperature, and finally Triton X-100 is added. Both CUBIC reagents should be degassed before use.

For whole-brain clearing, fixed brain samples were immersed in reagent 1 (10 g per brain) at 37°C for 3 days with gentle shaking. The solution was then exchanged, and the brain was immersed for an additional 3 to 4 days. At that point, if the white matter is not significantly cleared, further immersion with exchanged reagent 1 may be needed. The treated brain was washed with PBS several times at room temperature with gentle shaking, immersed in 20% (w/v) sucrose in PBS, degassed (required to prevent air bubbles from remaining in the ventricle), and immersed in reagent 2 (10 g per brain) for 2 to 7 days. Further immersion increased the final transparency but also caused swelling of the sample. After imaging, the sample was again washed with PBS, immersed in 20% (w/v) sucrose in PBS, and stocked in O.C.T. compound at -80°C. For nuclear staining with SYTO 16 (Life Technologies), 0.25 to 2 μM of the stain (depending on sample size) was added during reagent 1 treatment. For nuclear staining with propidium iodide (PI, Life Technologies), 10 μg/mL of the stain was added during reagent 1 treatment. After the step, additional staining was needed: sample was subjected to a freeze-thaw step followed by further incubation in 10 μg/mL of PI/PBS for 3 days at 37°C with rotation. Then, the solution was exchanged followed by staining for an additional 3 days.

3D Immunostaining of CUBIC Samples

A fixed brain block was treated with reagent 1 for 3 to 6 days, washed with PBS, immersed in 20% (w/v) sucrose in PBS, and frozen in O.C.T. compound at -80°C overnight. The frozen sample was then thawed, washed with PBS, and subjected to immunostaining with the primary antibodies in 750 μl of 0.1% (v/v) Triton X-100, 0.5% (w/v) bovine serum albumin, 0.01% (w/v) sodium azide in PBS for 3 days at 37°C with rotation. The stained samples were then washed with 10 ml of 0.1% (v/v) Triton X-100 in PBS several times at 37°C with rotation and then stained with the secondary antibodies in 750 μl of 0.1% (v/v) Triton X-100, 0.1% (w/v) bovine serum albumin, 0.01% (w/v) sodium azide in PBS for 3 days at 37°C with rotation. The stained samples were then washed with 10 ml of 0.1% (v/v) Triton X-100 in PBS several times at 37°C with rotation, immersed in 20% (w/v) sucrose in PBS, degassed, and immersed in reagent 2 for 24 to 36 hr. Note that longer treatment with reagent 2 may cause nonspecific signals in the void structures such as vessels and ventricles. The following antibodies were used for the staining: rabbit anti-VIP (Immunostar 20077, 1:300), goat anti-Copeptin (Santa Cruz Biotechnology sc-7812, 1:100), rabbit anti-Synapsin I (Millipore AB1543P, 1:250), donkey anti-rabbit Alexa 647 and anti-goat Alexa 546 (Life Technologies, 1:750 each). These antibodies were mixed with the sample after filtration with an Ultrafree-MC GV Centrifugal Filter (Millipore UFC30GV00). We have succeeded in the efficient 3D-IHC of all antibodies in our study. Although we have not yet encountered less effective antibodies, we could not exclude the possibility of impaired immunostaining resulting from the urea denaturation. The most important point may be that the antibodies are polyclonal. Also, peptide antibodies such as rabbit anti-VIP and goat anti-Copeptin would minimize the urea denaturation effect. On the other hand, in case of the antibodies recognizing a specific protein conformation, the urea denaturation may critically inhibit the antigen-antibody reaction. In our protocol, the fixed hypothalamus block was incubated in the antibody cocktail for 3 days at 37°C. In Figure 4C and the right panel of Figure S4C, we found that AVP immunoreactive signal was observed in the depth of at least 800 μm. Therefore, the kinetics of penetration can be conservatively estimated at ~270 μm/day at 37°C. Although VIP signal was not observed in the depth of 750 μm, the result was consistent with previous reports that VIP fibers were terminated around the subparaventricular region (Abrahamson and Moore, 2001).

Microscopy

Whole-brain fluorescence images were acquired with light-sheet fluorescence microscopy (LSFM) (Ultramicroscope, LaVision BioTec, Germany), combined with 488 nm and 588 nm lasers (Coherent Sapphire488LP-100 and Sapphire588LP-50), a sCMOS camera (Andor Neo 5.5) and a macrozoom microscope (Olympus MVX-ZB10) with 0.63 × objective lens (Olympus MVPLA00.63X, NA = 0.15, working distance = 87 mm) (Figure S3A). The camera and the microscope were connected to a camera adaptor (Olympus MVX-TV1X), tube lens (Olympus MVX-TLU), and the Ultramicroscope filter wheel unit (LaVision BioTec, emission filters: ET525/50 and ET650/60), with adaptors (LaVision BioTec, LV AD MVX_1 and LV AD MVX_2). Samples were immersed in a 1:1 mixture of silicon oil TSF4300 (Momentive Performance Materials, RI = 1.498) and mineral oil (Sigma-Aldrich, RI = 1.467) during image acquisition.

Images were captured using 2 × zoom (for mouse brain) and 1 × zoom (for marmoset brain) with the MVX-ZB10. When 2 × zoom was used, the theoretical X-Y resolution of acquired image is about 4.7 μm. We prepared a customized sample holder for capturing the image of a larger marmoset hemisphere and for easier sample handling. Each plane was illuminated from both the right and left sides, and a merged image was saved. The exposure times were adjusted according to the fluorescent signal intensities of each sample. We acquired 25 whole-brain images in total (4 × single-channel whole mouse brains taken from two directions, 4 × two color-channels whole mouse brains taken from two directions, 1 × single-channel marmoset hemisphere taken from one direction) for this study.

We quantified the level of background fluorescence in CUBIC samples (Figure 3F, 3G, 3H, and 3I). For the analysis, we used images from the R26-pCAG-nuc-3 × mKate2 mouse brain. First, we masked the regions outside the brain to precisely evaluate the background fluorescence inside the brain. To this end, we constructed the 3D NIfTI-1 image file for this brain and aligned the Waxholm-Space atlas (i.e., reference brain) to the brain. We then created a binary mask using the aligned atlas and applied it to the raw TIFF images so that all pixels that are not in an annotated region (i.e., pixels that fall outside the brain) have their intensity set to zero. We used pixels with nonzero value (i.e., inside the brain) of the resulting images for the subsequent analysis. This data set includes 646 horizontal slices, numbered from 0, so we then worked on slice 322, at the center of the brain (Figure 3F, left). Our initial step was to manually determine two thresholds that separate the low-intensity signal (smaller than 8100), medium-intensity signal (between 8100 and 35000) and high-intensity signal (greater than 35000). This was obtained by extracting these regions from the raw image (left), normalizing the three resulting images and assigning each to a channel of the false-color RGB image. We color-coded these signals in blue, green and red, respectively (Figure 3F, middle). This identifies very distinct regions, and background fluorescence is in the blue region, and appears well-below the signal of interest, in the green and red regions. This is confirmed in the right panel of Figure 3F, where all pixels with an intensity below 8100 are set to black. The background is visibly removed, while the real fluorescence signal is unaffected. To obtain more reliable background fluorescence levels while avoiding edge effects, we extended this result to slices 161–483 (50% of the total data). The background fluorescence level was associated with a peak in the low-intensity region of the image histogram, shown in Figure 3G for three slices (161, 322 and 483). For example, the peak of the background fluorescence is at intensity 7,616 for slice 322. Based on these histograms and on Figure 3F, we estimated that most background pixels have an intensity no more than 5% higher than this peak intensity ($7616 + 5\% = 7996.8$). We therefore used this threshold (5% higher than the background peak), and considered intensity above this threshold as signals (e.g., 50th percentile of the signal intensity corresponds the median intensity for pixels between this threshold and the maximum intensity). We repeated this analysis for other slices 161–483, and showed 95th, 80th, 65th, and 50th percentile of the signal intensity as well as the peak intensity of the background fluorescence in Figure 3H. We also calculated the ratio between each percentile of the signal intensity and the peak intensity of the background fluorescence (Figure 3I), which indicates that the fluorescence signal is significantly brighter than the background peak.

Immunostained SCN and cerebral cortex images were acquired with an inverted confocal microscope (Leica TCS SP8) with 10 × (Leica PL APO CS, NA = 0.40, working distance = 2.2 mm) or 20 × (Leica PL APO CS2, NA = 0.75, working distance = 0.68 mm) objective lenses, and with another inverted confocal microscope (Carl Zeiss LSM700) with a 10 × (Plan Aplanachromat, NA = 0.45, working distance = 2.1 mm) objective lens. To detect most of the stained signals in the unsaturated range of intensity, laser output was gradually increased according to the Z-stack acquisition.

Arc-dVenus Tg brain images in Figure S6A were captured with fluorescence stereomicroscopy using the same settings as previously described (Eguchi and Yamaguchi, 2009). Two-photon imaging was performed using an upright multiphoton microscope (Olympus FV1000, BX61WI) combined with a MaiTai DeepSee HP-OL laser (Spectra Physics) and a 25 × objective lens for Scale (Olympus, XLSLPLN25XSVMP, NA = 0.9, working distance = 8 mm) for Figure 2D and S2, or using another upright multiphoton microscope (LSM7MP, Carl Zeiss) combined with a MaiTai DeepSee laser (Spectra Physics) and a 25 × objective lens (Olympus XLPLN25XWMP, NA = 1.05, WD = 2 mm) for Figure S5B.

Image Data Processing

All raw image data were collected in a lossless TIFF format (16-bit images for LSFM and two-photon microscopy data, and 8-bit images for confocal microscopy data). 3D-rendered images were visualized and captured with Imaris software (version 7.6.4, Bitplane). Brightness, contrast, and gamma of the 3D-rendered images were manually adjusted with the software at minimum when visualized. Confocal and two-photon 2D images as well as a projection image of Thy1-YFP-H brain (Figure S5A) were processed and visualized with Fiji (<http://fiji.sc/Fiji>). Z-projection (maximum intensity) was performed to stack 2 to 21 sequential images with the software. Brightness and contrast were manually adjusted at minimum when visualized. Gaussian filtering was performed on the image in Figure S5B.

To facilitate the dissemination of neuroinformatics tools, the Neuroimaging Informatics Technology Initiative (NIFTI) introduced the NIfTI-1 data format (.nii extension), which is now supported by most major software packages. Detailed specifications are available on the Initiative's website: <http://nifti.nimh.nih.gov/nifti-1/>. The computational analysis described below relies on this format. NIfTI-1 files were visualized using ITK-SNAP (Yushkevich et al., 2006) (Figure 7 and S7).

To generate a NIfTI-1 file from each stack of TIFF images obtained from LSFM, we first converted the images to 16-bit PNG files using *ImageMagick*. During this conversion, we also downscaled to 25% (i.e., keeping one of every four images and changing the resolution of these images from 2560 × 2160 to 640 × 540). This was necessary because of memory limitations of the current

software tools. Using the *Convert3D* tool from ITK-SNAP, each temporary stack was converted to a NIfTI-1 file, specifying the correct spacing ($0.02064 \times 0.02064 \times 0.04$ mm, given the downscaling) and the correct orientation (which depended on the acquisition direction). Each resulting NIfTI-1 file was visualized and manually checked for size and orientation. These NIfTI-1 files were the input for the subsequent computational analysis.

The reference atlas used in our analysis was the Waxholm Space Atlas (Johnson et al., 2010). The Canon T1 image was downloaded from the website of the International Neuroinformatics Coordinating Facility: <http://software.incf.org/software/waxholm-space>, and downscaled to $216 \times 512 \times 256$ (again for memory concerns in subsequent steps). Spacing was adjusted accordingly. To remove surrounding nonbrain tissue, this image was then multiplied by a binary mask calculated from the WHS annotation labels (using *Convert3D*), so that only labeled areas, (i.e., only brain regions), were conserved in the atlas NIfTI-1 file used for registration, as detailed below.

The CUBIC Informatics

To facilitate analysis across samples, whole-brain images are registered and aligned to reference structures. In our analysis, we aligned images by pairs, in which one image corresponded to the structural information (obtained via nuclear staining) and the other to the signal channel. For each pair, we performed two steps: (i) registration of the structural information to a reference, and (ii) alignment of both images, i.e., applying the transformation (calculated during the registration) to both the structural image and the signal channel image (Figure 7A).

Image registration is a very active field of research, (see e.g., (Avants et al., 2011; Woods et al., 1992)). Here, we use ANTs (Advanced Normalization Tools), which has proved successful in a number of image registration tasks (Murphy et al., 2011). When aligning our composite images with each other or to the Waxholm Space Atlas, we use affine transformations only (with mutual information, 64 bins and 300000 samples as the parameters of the ANTS function). When aligning images of the same brain obtained from opposite acquisition directions, as part of the image composition process, we allowed small nonlinear transformations to overcome differences in sharpness. These nonlinear transformations were calculated in ANTs using SyN, the symmetric normalization model (Avants et al., 2008; Klein et al., 2009). The affine parameters were unchanged, and we used $10 \times 10 \times 10$ iterations for SyN. One file was generated for each transformation. Nonlinear transformations are not compulsory: it is also possible to use affine transformations only for this step. The results shown in Figure 7 did not use SyN. Finally, alignment was performed using the *WarpImageMultiTransform* function and the computed transformations above as parameters (i.e., the affine transformation if using affine registration only, or both the affine transformation and the diffeomorphic transformation otherwise).

The overall analysis process is summarized in Figure S7A. We first aligned and combined images of the same brain acquired from opposite directions. We then aligned these composite images to an internal reference and to the Waxholm Space Atlas. Finally, we compared the signal channel images of different brains, e.g., by subtracting them [using the *fslmaths* function from FSL (Jenkinson et al., 2012)] to highlight differences in expression in specific regions (Figures 7D and 7E).

When images from two acquisition directions were available for the same brain, combining them into a single composite 3D image ensured optimal sharpness of the 3D image throughout the brain. This was motivated by the fact that, in images taken in the ventral-to-dorsal (V-D) direction, the ventral horizontal slices were sharper, while in images taken in the dorsal-to-ventral (D-V) direction, the dorsal horizontal slices were sharper, (Figure S7C). When comparing two images of the same object, the image with more edges can be considered sharper. We therefore estimated via the Sobel operator (Gonzalez and Woods, 2002) the “edge content” of each horizontal plane of the D-V and V-D 3D images of the same brain. This operation defined two unique values, n and m , such that the relative difference in “edge content” was below 10% for planes between n and m , (Figure S7D). We respectively noted S_i^{VD} and S_i^{DV} , the horizontal slice number i from the V-D image and the D-V image previously aligned to the V-D image. We could then construct the composite 3D image, one horizontal slice at a time, with the weighted sum $S_i^{COMP} = w \times S_i^{DV} + (1 - w) \times S_i^{VD}$ and weights w defined as follows: $w = 0$ if $i \leq n$, $w = 1$ if $i \geq m$ and $w = i / (m - n) + n / (n - m)$ otherwise. The resulting image was sharp throughout the brain, (Figure S7E). We implemented the operator and the weighted sum to operate on matrices containing raw intensity values. To obtain these values from the NIfTI-1 files, and then to export the results back to the NIfTI-1 format, we used the FSL functions *fsl2ascii* and *fslascii2img*, respectively.

SUPPLEMENTAL REFERENCES

Avants, B.B., Epstein, C.L., Grossman, M., and Gee, J.C. (2008). Symmetric diffeomorphic image registration with cross-correlation: Evaluating automated labeling of elderly and neurodegenerative brain. *Med. Image Anal.* 12, 26–41.

Gonzalez, R.C., and Woods, R.E. (2002). *Digital image processing*, Second Edition (Reading, MA: Prentice Hall).

Jenkinson, M., Beckmann, C.F., Behrens, T.E., Woolrich, M.W., and Smith, S.M. (2012). *Fsl*. *Neuroimage* 62, 782–790.

Kiyonari, H., Kaneko, M., Abe, S., and Aizawa, S. (2010). Three inhibitors of FGF receptor, ERK, and GSK3 establishes germline-competent embryonic stem cells of C57BL/6N mouse strain with high efficiency and stability. *Genesis* 48, 317–327.

Klein, A., Andersson, J., Ardekani, B.A., Ashburner, J., Avants, B., Chiang, M.C., Christensen, G.E., Collins, D.L., Gee, J., Hellier, P., et al. (2009). Evaluation of 14 nonlinear deformation algorithms applied to human brain MRI registration. *Neuroimage* 46, 786–802.

- Kuwajima, T., Sitko, A.A., Bhansali, P., Jurgens, C., Guido, W., and Mason, C. (2013). *Clear^T*: a detergent- and solvent-free clearing method for neuronal and non-neuronal tissue. *Development* *140*, 1364–1368.
- Morell, P., and Quarles, R.H. (1999). Characteristic composition of myelin. In *Basic Neurochemistry: Molecular, Cellular and Medical Aspects* 6th edition, G.J. Siegel, B.W. Agranoff, R.W. Albers, et al., eds., (Philadelphia: Lippincott-Raven), <http://www.ncbi.nlm.nih.gov/books/NBK28221/>.
- Tsai, P.S., Kaufhold, J.P., Blinder, P., Friedman, B., Drew, P.J., Karten, H.J., Lyden, P.D., and Kleinfeld, D. (2009). Correlations of neuronal and microvascular densities in murine cortex revealed by direct counting and colocalization of nuclei and vessels. *J. Neurosci.* *29*, 14553–14570.
- Tsujino, K., Narumi, R., Masumoto, K.H., Susaki, E.A., Shinohara, Y., Abe, T., Iigo, M., Wada, A., Nagano, M., Shigeyoshi, Y., and Ueda, H.R. (2013). Establishment of *TSH β* real-time monitoring system in mammalian photoperiodism. *Genes Cells* *18*, 575–588.
- Woods, R.P., Cherry, S.R., and Mazziotta, J.C. (1992). Rapid automated algorithm for aligning and reslicing PET images. *J. Comput. Assist. Tomogr.* *16*, 620–633.

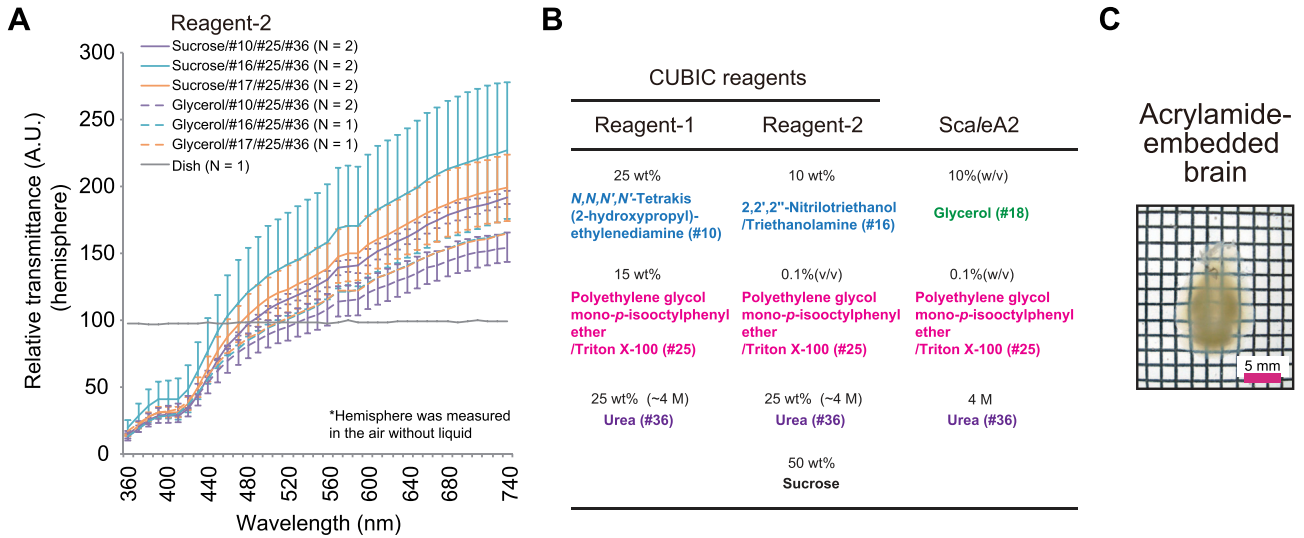


Figure S1. Development of CUBIC Reagents by Comprehensive Chemical Screening, Related to Figure 1

(A) Development of reagent 2, a high RI version of reagent 1. Reagent 2 candidate solutions contained 50 wt% sucrose or glycerol, 25 wt% urea, 10 wt% of an aminoalcohol and 0.1% (v/v) Triton X-100. Fixed mouse hemispheres were treated with reagent 1 (#10/#25/#36) for 5 days, washed with PBS, and immersed in each reagent 2 for 24 hr. The refractive indices of sucrose- or glycerol-containing reagent 2 were 1.48–1.49 and 1.45–1.46, respectively. After the incubation of reagent-1-treated hemispheres with the various reagent 2 candidate solutions, transmittance (360–740 nm) was measured as in Figure 1E. Sucrose-based solutions resulted in higher transmittance values than glycerol-based solutions, and 2,2',2''-nitrilotriethanol/triethanolamine (#16) tended to clear the samples more reproducibly than the other tested aminoalcohols. Note that some of the values exceeded 100 as in Figure 1E (see Extended Experimental Procedures for the details). The values represent the average \pm SEM from two independent samples. (B) Recipes of CUBIC reagents and ScaleA2. Aminoalcohols were chosen in place of glycerol. We referred to the concentration of urea (#36) in ScaleA2 (4 M) for determining its concentration in CUBIC reagents (25 wt%). However, it was calculated as wt% for ease of preparing the mixtures. Other components were added as much as possible, considering fluorescence signals and viscosity. (C) CUBIC clearing using an acrylamide-embedded brain prepared according to the CLARITY protocol. The reagent 1 and 2 were used to clear an acrylamide-embedded mouse brain (Chung et al., 2013). Although the clearing was less efficient compared to the results using “fix-only” samples (Figure 2A), the protocol could be applied to the polymer-embedded sample.

SCALEVIEW-A2

Thy1-YFP-H hemisphere
treated for 3 days at 37°C

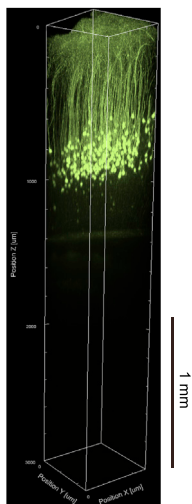


Figure S2. Two-Photon Deep Brain Imaging of a SCALEVIEW-A2-Treated Thy1-YFP-H Tg Hemisphere, Related to Figure 2

Two-photon deep brain imaging of Thy1-YFP-H Tg hemisphere, treated with commercially available Sca/eA2 solution (SCALEVIEW-A2 from Olympus) as in the same condition of Figure 2D (for 3 days at 37°C). The resulting sample was observed using two-photon microscopy as in Figure 2D. The performance of Sca/eA2 in a Thy1-YFP-H Tg brain after treatment for 7 days is found in the Sca/e original paper (Hama et al., 2011), and recent update of Sca/e technology will be available at <http://cfds.brain.riken.jp>.

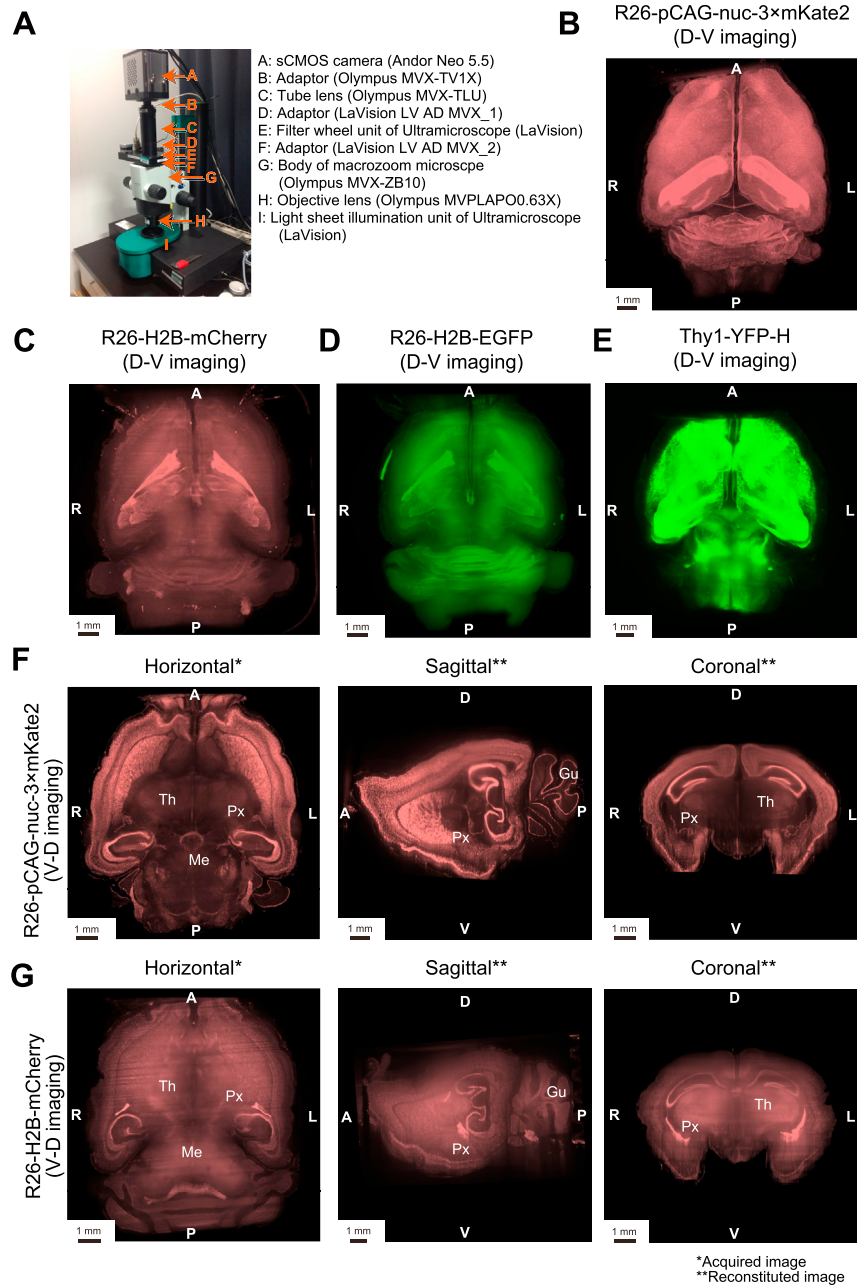


Figure S3. Details of the CUBIC Application to Rapid Whole-Brain Imaging of Various Fluorescent Proteins, Related to Figure 3

(A) Setup of the light-sheet fluorescent microscopy (LSFM) equipment used in this study. (B) The R26-pCAG-nuc-3 × mKate2 mouse brain (from a 5-week-old mouse) shown in Figure 3A and 3B. Images were acquired from the dorsal to ventral (D-V) direction and depicted from the ventral side in order to directly compare with Figure 3. Z-stack: 10- μ m step \times 646 planes, with 0.28 s \times two illuminations. (C) D-V image of the R26-H2B-mCherry mouse brain (from a 6-month-old mouse) shown in Figure 3C. Z-stack: 10- μ m step \times 696 planes, with 4 s \times two illuminations. (D) D-V image of the R26-H2B-EGFP mouse brain (from a 6-month-old mouse) shown in Figure 3D. Z-stack: 10- μ m step \times 667 planes, with 4 s \times two illuminations. (E) D-V image of the Thy1-YFP-H Tg mouse brain (from a 2-month-old mouse) shown in Figure 3E. Z-stack: 10- μ m step \times 733 planes, with 0.3 s \times two illuminations. (F) and (G) Selected acquired horizontal images and reconstituted sagittal and coronal images of the R26-pCAG-nuc-3 × mKate2 knockin brain (V-D imaging) and the R26-H2B-mCherry knockin brain (V-D imaging) shown in Figure 3A – 3B and 3C, respectively. Both of the genes were knocked into the same ROSA26 locus but were regulated by different promoters (the CAG promoter versus the endogenous ROSA26 promoter). The expression patterns of these proteins were compared with the corresponding reconstituted sections. Areas of differential expression are indicated. Th, thalamus; Px, ventricular choroid plexus; Me, medulla; Gu, granular layer of cerebellum. A, anterior; P, posterior; R, right; L, left; D, dorsal; V, ventral.

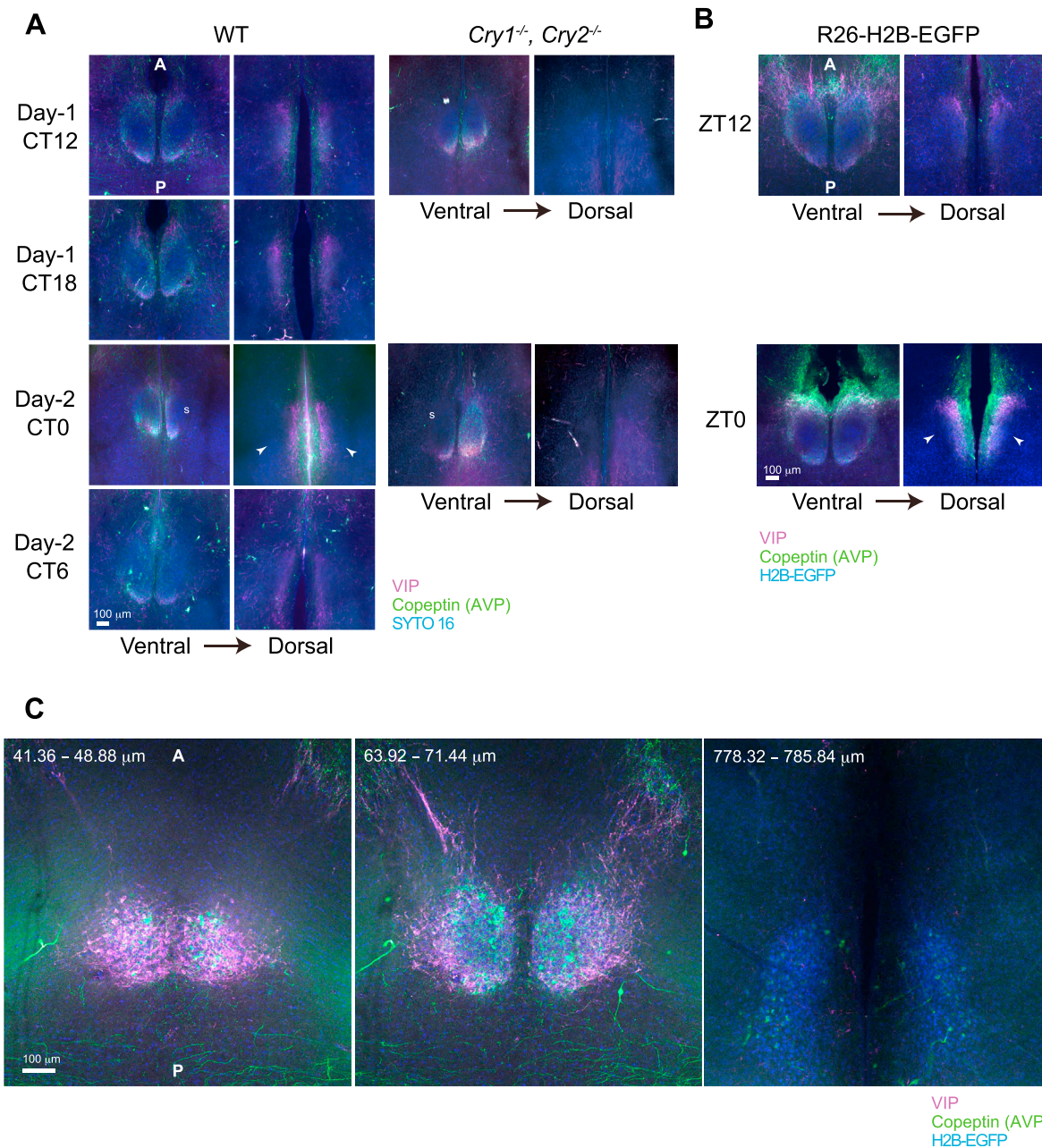


Figure S4. Reproducibility in the Application of CUBIC to the Adult Brain Imaging of 3D Immunostained Samples, Related to Figure 4

(A) An independent set of 3D-IHC imaging results corresponding to Figure 4D is shown. WT and *Cry1^{-/-}, Cry2^{-/-}* samples were stained with antibodies to VIP and Copeptin. Staining of both the WT and *Cry1^{-/-}, Cry2^{-/-}* SCN (day-2, CT0) was partially incomplete due to a scar in the sample (indicated as “s” in the ventral images). (B) The R26-H2B-EGFP mice housed under 12 h:12 hr light-dark conditions were sacrificed at the indicated zeitgeber time (ZT), and the fixed brains were subjected to a similar 3D-IHC analysis. Consistent with the results in Figure 4D, the dorsal fibers close to the third ventricle were more strongly stained at ZT0 than ZT12. In both panels, the depth of the horizontal images is approximately 140 μm on the ventral side and 290 μm on the dorsal side (Z-projection with maximum intensity, 1.98-μm step × 3 planes in (A) and 3.76-μm step × 2 planes in (B) from the most ventral plane of the SCN region. Strong signals of the neuropeptides detected in the dorsal side of SCN at CT0/ZT0 are indicated with arrowheads. (C) Enlarged 3D-IHC analysis images of the other R26-H2B-EGFP mice SCN (left and middle panels) and PVN (right panel), sacrificed at the ZT12 (Z-projection with maximum intensity, 3.76-μm step × 2 planes). Images were acquired and processed in a similar but an optimized condition for each sample so that most of the stained signals were obtained in the unsaturated range of intensity.

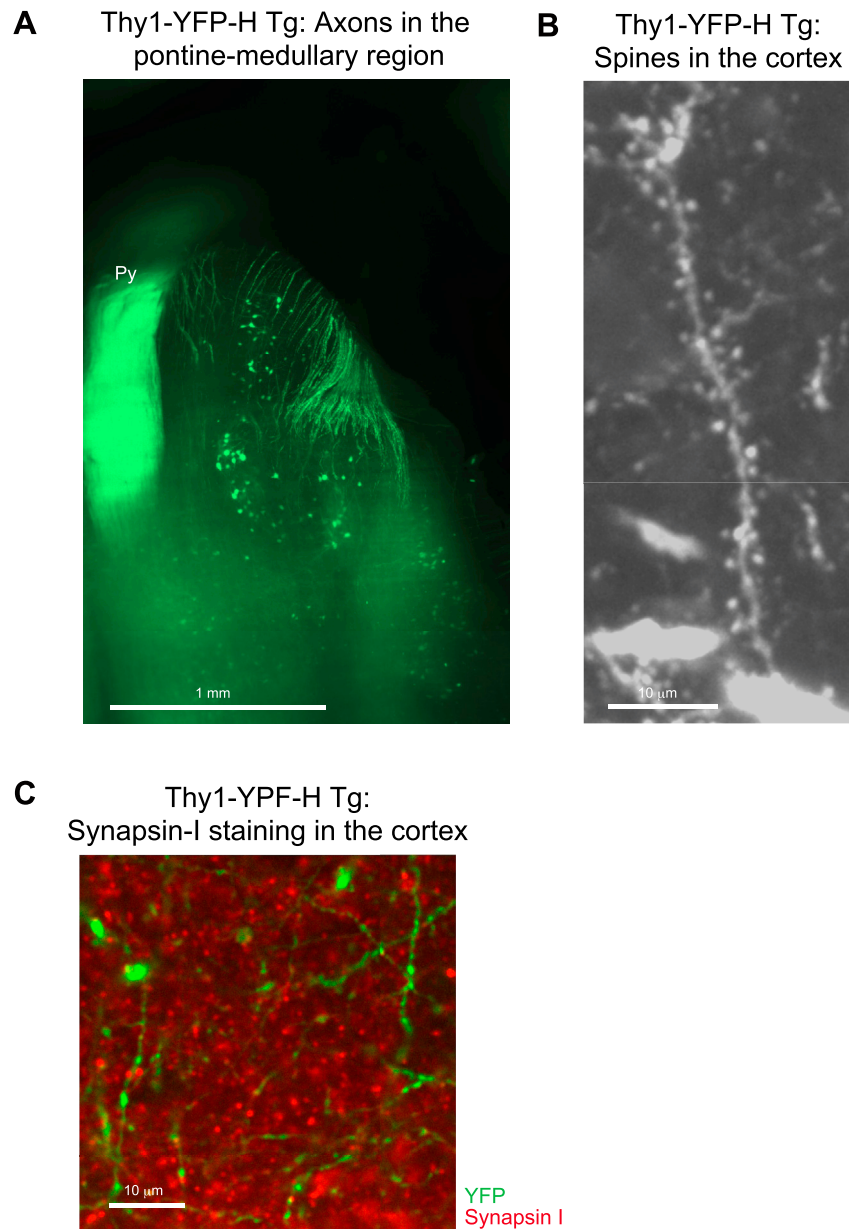


Figure S5. CUBIC Is Scalable in Its Application to Subcellular Structure Imaging, Related to Figure 5

(A) Axons in the pontine-medullary region of the Thy1-YFP-H Tg CUBIC brain sample, observed with LSFM. The image is a part of the Z-projection image of the V-D YFP channel imaging data shown in Figure S7B (Z-projection with maximum intensity, 10- μ m step \times 21 planes). Py, pyramidal tract. (B) Spines in the cerebral cortex of the Thy1-YFP-H Tg CUBIC brain sample, observed with two-photon microscopy. The image is part of the Z-projection image of two-photon imaging data (Z-projection with maximum intensity, 0.5- μ m step \times 20 planes). (C) Immunostaining with a Synapsin-I antibody in the cerebral cortex of the Thy1-YFP-H Tg CUBIC brain sample, observed with confocal microscopy. Part of an original acquired image is shown.

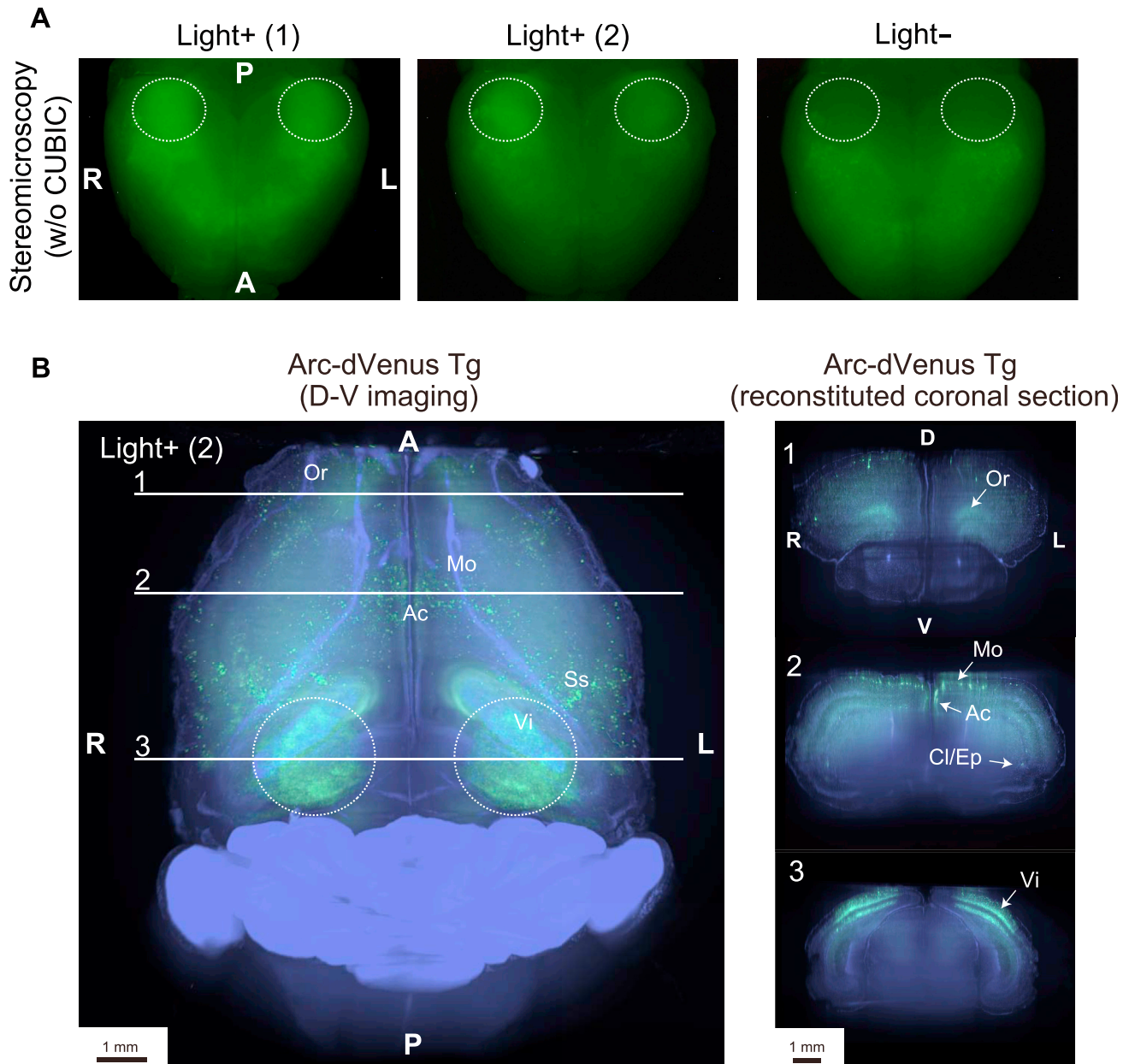


Figure S6. Whole-Brain Nuclear Counterstaining in CUBIC Enables the Visualization of Neural Activities Induced by Environmental Stimulation, Related to Figure 6

(A) Venus signals (green) of Arc-dVenus Tg mouse brains, which were used for Figure 6 and S6B, were also observed with fluorescent stereomicroscopy. A region including the visual area in the cortex is indicated by a dotted ellipse, encompassing the area where the Venus signals appeared in Light+ brains. (B) The Light+ (2) Arc-dVenus Tg mouse brain was subjected to CUBIC treatment, and two-color D-V images were acquired with LSFM (Z-stack: 10- μ m step \times 633 planes) as in Figure 6B. Increased fluorescent signals were observed in the same regions as observed in the Light+ (1) brain shown in Figure 6B.

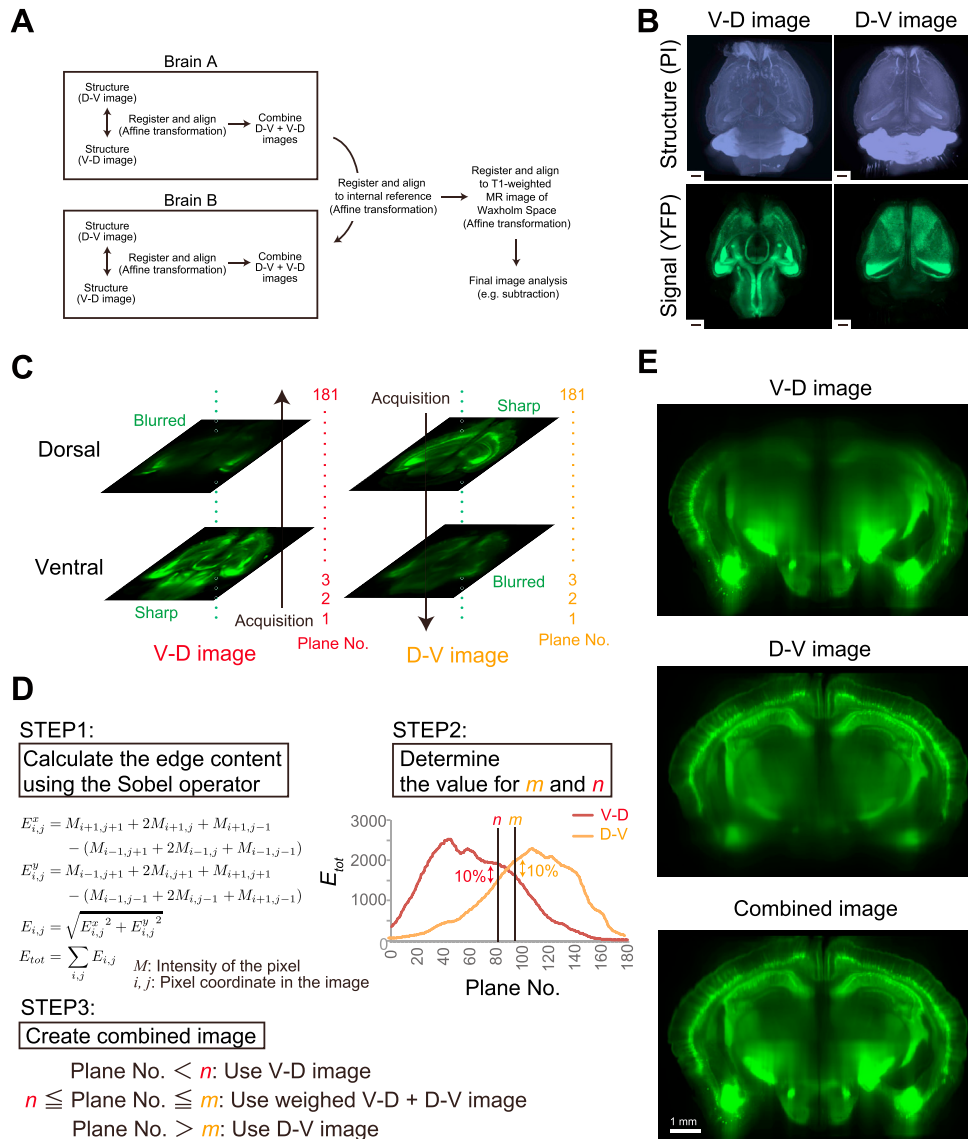


Figure S7. Computational Image Analysis in CUBIC Enables Gene Expression Profiling of Adult Whole Brains, Related to Figure 7

(A) Overview of computational analysis steps. For each brain, we first combined imaging data acquired in the ventral-to-dorsal (V-D) and dorsal-to-ventral (D-V) directions. To do so, we first aligned the D-V and the V-D brain images and then considered the sharpness of each horizontal plane to generate a single clear 3D image as in (C)–(E). These samples were then aligned to an internal reference brain, and to a reference atlas. This was achieved by registering the image containing structural information, and then applying the corresponding transformation to both the structural and the signal image of the same brain. Finally, the aligned signal images were compared and contrasted using methods such as subtraction, to highlight differences between samples. (B) A data set consisting of reconstituted 3D images acquired from a single Thy1-YFP-H Tg mouse brain subjected to whole-brain nuclear counterstaining with PI is shown. Structural information obtained by PI staining was used to calculate the transformation matrix. Z-stack: 10- μ m step \times 722 planes for V-D imaging and 10- μ m step \times 797 planes for D-V imaging, with 0.6 s \times two illuminations for YFP and with 0.15 s \times two illuminations for PI, respectively. Scale bar: 1 mm. (C) Image sharpness depended on acquisition directions. The raw data in (B) were converted to a NIFTI-1 file for further analysis. We downsampled original image data to 25% (i.e., keeping one of every four images and changing the resolution of these images from 2560 \times 2160 to 640 \times 540). During conversion, the same plane number was assigned to equivalent planes of both images. In this case, the ventral horizontal planes were sharper in the V-D image, while dorsal horizontal planes were sharper in the D-V image. The images obtained in two directions were combined to obtain a single clear 3D image. (D) Estimating the edge content to combine the two acquisition directions. A classic edge detection method is to use the Sobel operator (noted $E_{i,j}$ here), which corresponds to a gradient estimation at pixel (i, j) of an image. Summing this value over all pixels of the image gives us the edge content E_{tot} of the image. Plotting E_{tot} as a function of the plane number, for the V-D and D-V images, confirms the observation from (C). If we note these values E_{VD} and E_{DV} , respectively, we can define a unique range $[n, m]$ where $|E_{VD} - E_{DV}| / E_{VD} < 0.1$. Finally, the values for n and m are used to design a weighted sum of the V-D and D-V images (see [Extended Experimental Procedures](#)). (E) Combining the compensated V-D and D-V images from a single Thy1-YFP-H brain (NIFTI-1 file). $n = 87$, $m = 93$.